

# Towards Variational Quantum Algorithms for generalized linear and nonlinear transport phenomena

Sergio Bengoechea<sup>a,\*</sup> , Paul Over<sup>a</sup> , Dieter Jaksch<sup>b,c</sup>  and Thomas Rung<sup>a</sup> 

<sup>a</sup> Institute for Fluid Dynamics and Ship Theory, Hamburg University of Technology, 21073 Hamburg, Germany;

<sup>b</sup> Institute for Quantum Physics, University of Hamburg, Luruper Chaussee 149, 22761 Hamburg, Germany;

<sup>c</sup> Clarendon Laboratory, University of Oxford, Parks Road, Oxford OX1 3PU, United Kingdom;

## Keywords

Computational Fluid Dynamics, Variational Quantum Algorithms, Quantum Computing, Convection Schemes

## Abstract

This article proposes a Variational Quantum Algorithm (VQA) to solve linear and nonlinear thermofluid dynamic transport equations. The hybrid classical-quantum framework is applied to problems governed by the heat, wave, and Burgers' equation in combination with different engineering boundary conditions. Topics covered include the consideration of non-constant material properties and upwind-biased first- and higher-order approximations, widely used in engineering Computational Fluid Dynamics (CFD), by the use of a mask function. The framework is able to convert band matrices arising from Partial Differential Equations (PDEs) discretized on structured grids into quantum gates, thus contributing to the development of a modular library for quantum computing translations of CFD procedures. Verification examples demonstrate high predictive agreement with classical methods. Furthermore, the scalability analysis shows a *polylog* complexity in the number of qubits of the quantum circuits involved. Remaining challenges refer to the implicit construction of upwind schemes.

## I. INTRODUCTION

Computational Fluid Dynamics (CFD) has been established as a central discipline in computational science and engineering with applications ranging from climate research, to energy conversion or transportation and biomedical industries. The interest in numerical resolution of larger spatial and temporal scales encounters

---

\* Corresponding author.

E-mail address: sergio.bengoechea@tuhh.de

extremely expensive and energy-intensive simulations on classical hardware [1]. In this respect, Quantum Computers (QCs) promise a computational potential that cannot be achieved by classical hardware [2].

The research field of Quantum CFD (QCFD) is rapidly growing and can be divided into quantum-inspired approaches [3]–[5], that are not necessarily implemented on quantum hardware, and methods that are closely oriented to the capabilities and restrictions of quantum hardware [6]–[23]. This work is focused on the second type of methods and their application to CFD.

Steijl and Barakos [6] used a hybrid classical-quantum approach for solving the Poisson problem in the vortex-in-cell method via a quantum Fourier algorithm. A similar strategy is employed in the work of Cao et al. [7] to approximate the Poisson equation in the predictor-corrector solver of the incompressible Navier-Stokes equation. Here, the Quantum Linear Solver of Equations (QLSE) proposed by Harrow, Hassadim, and Lloyd (HHL) [8] is applied. In Ref. [9] and [10], the Quantum Amplitude Estimation Algorithm (QAEA), described by Kacewicz [11], solves the system of coupled Ordinary Differential Equations (ODEs), following the spatial discretization of the Navier-Stokes and the Burgers' equation, respectively. The incremental time application of the HHL method is employed in Ref. [12] to approximate compressible flows after discretizing the Navier-Stokes equation with classical finite volumes. Another methodology employs the Hamiltonian simulation for transport problems as it has been proposed by Brearley et. al [13] and Over et. al [24] for the advection and the advection-diffusion equation, respectively. Instead of the QLSE approach, the system dynamics of the discrete problems are herein unitarized for a time evolution strategy, which is suitable for QCs. Unfortunately, these algorithms have to devote a range of qubits to error corrections, which significantly increases the total qubit count. Therefore, these algorithms are more appropriate for future fault-tolerant QC than for the current Noise Intermediate-Scale Quantum (NISQ) era [14], [15].

Variational Quantum Algorithms (VQAs) provide an alternative for solving CFD problems on NISQ devices. VQA procedures rely on the combination of classical and quantum hardware, and require reformulating the governing Partial Differential Equation (PDE) as an optimization problem. The QC part of the employed hardware is dedicated to efficiently evaluating the cost function, while the classical hardware drives the optimizer for the parameterized solution. VQAs employ shallow circuits with a small number of gate operations, thereby reducing potential decoherence errors. Recent applications of VQAs on fluid dynamics are reported in Refs. [16]–[23]. Some of these approaches are inspired by Physics Informed Neural Networks (PINNs), where quantum neural networks are trained variationally [16] to solve the Navier-Stokes equation for supersonic nozzle flows. In contrast, the work of Demirdjian et al. [17] separates the discretized Burgers' advection-diffusion equation in a finite series of unitary operations that are approximated with the variational quantum linear solver introduced in Ref. [18]. In Sato et al. [19], the potential energy minimization of the elliptic Poisson equation is treated with a VQA that linearly decomposes the equation's dynamics in a series of parameterized quantum circuits. The energy minimization approach of Sato et al. [19] is adapted to time-dependent problems in Leong et al. [20]–[22]. The work of Over et al. [23] extends the Hadamard test-based VQA, described in Lubasch et al. [25], to

the treatment of PDEs in combination with a variety of engineering boundary conditions.

The present investigation extends the scope of Ref. [23] to more general nonlinear convection-diffusion-reaction problems in combination with a variety of engineering boundary conditions. To this end, different approximations of convective kinematics frequently used in engineering CFD, such as Central-Differencing-Scheme (CDS), Upwind-Differencing-Scheme (UDS) or the higher-order Linear-Upwind-Differencing-Scheme (LUDS), and Quadratic-Upstream-Interpolation-for-Convective-Kinematics (QUICK), are integrated into the VQA framework, additionally the occurrence of inhomogeneous material properties is also considered. The aforementioned studies are based on a general framework of encoding arbitrary band matrices in the Hadamard-based VQA [25], maintaining an efficient implementation with optimal gate complexity in the number of qubits. The publication is structured as follows: Section II describes the mathematical model and outlines the reformulation of the PDE into a minimization problem. The general layout of the VQA and its major building blocks are explained in Sec. III, while Sec. IV provides details of the quantum circuits representing the upwind-biased convective kinematics as well as the inhomogeneous material properties including the related complexity analysis. VQA-results obtained for the wave, heat, and Burgers' equations are compared with classical approaches in Sec. V and Sec. VI is devoted to conclusions. The quantum circuits presented in this study have been emulated with IBM's QISKIT environment v.0.42.1 [26], following a *little-endian* convention in the binary representation.

## II. MATHEMATICAL FRAMEWORK

The Section contains two major parts, i.e., the derivation of the discretized governing equations (Sections II-A, II-B), and the preparation of the corresponding optimization problem (Sec. II-C).

### A. Governing Equations

The presented approach is restricted to second-order linear and nonlinear PDEs, commonly appearing in CFD. The framework focuses on unsteady problems in one spatial dimension and extensions to more spatial dimensions are straightforward. We employ non-dimensional properties  $y = \tilde{y}/Y$ , where  $Y$  is a dimensional reference property, and use a dimensionless description of space  $\tilde{x} \in [\tilde{x}_0, \tilde{x}_1]$  and time  $\tilde{t} \in [0, T]$  with  $x = \tilde{x}/(\tilde{x}_1 - \tilde{x}_0) = \tilde{x}/L$  and  $t = \tilde{t}/T$ . Material properties are given by, the constant density  $\tilde{\rho} [kg/m^3]$ , the dynamic viscosity  $\tilde{\mu} [kg/ms]$ , the speed of sound  $\tilde{c} [m/s]$  and the thermal diffusivity  $\tilde{\alpha}(x) [m^2/s]$ . The governing equations describe the evolution of the dimensionless flow quantities referred to as the state  $y$ , i.e., the velocity  $v = \tilde{v}/V = \tilde{v}(T/L)$ , the temperature  $\vartheta = \tilde{\vartheta}/\vartheta_{\text{ref}}$ , and the pressure  $p = \tilde{p}/P$ .

A set of five non-dimensional similarity parameters  $a_i(x, t, y)$  that depend on space, time and state properties, are introduced together with a non-dimensional source term  $f$ , to formulate the dimensionless second-order

PDE, viz.

$$\begin{aligned}
a_1 \frac{\partial^2 y}{\partial t^2} + a_2 \frac{\partial y}{\partial t} - \frac{\partial}{\partial x} \left( a_3 \frac{\partial y}{\partial x} \right) + a_4 \frac{\partial y}{\partial x} + a_5 y &= f & \text{in } \Omega_T := (0, 1) \times (0, T], \\
y(x, t) &= y_{\text{BC}} & \text{on } \partial\Omega, \\
y(x, t) &= y_0 & \text{at } t = 0.
\end{aligned} \tag{1}$$

The coefficients  $a_i$  depend on the governing equation, cf. Tab. I. For the example of the non-dimensional Burgers' equation, the state refers to  $y = v$  and the coefficients follow from  $a_1 = 0$ ,  $a_2 = 1$ ,  $a_3 = 1/Re$ ,  $a_4 = v$  and  $a_5 = 0$ , where  $Re = \bar{\rho}VL/\bar{\mu}$  is the *Reynolds* number. The transient heat conduction problem ( $y = \vartheta$ ) is recovered from  $a_1 = 0$ ,  $a_2 = 1$ ,  $a_3 = \alpha(x)$ ,  $a_4 = 0$  and  $a_5 = 0$ , where the dimensionless thermal diffusivity  $\alpha(x) = \tilde{\alpha}(x)/(VL)$  varies in space. For modeling the propagation of sound ( $y = p$ ), a hyperbolic setting is recovered by choosing  $a_1 = Ma^2$ ,  $a_2 = 0$ ,  $a_3 = 1$ ,  $a_4 = 0$  and  $a_5 = 0$ , where  $Ma^2 = V^2/\tilde{c}^2$  is the square of the *Mach* number.

TABLE I: Key coefficients  $a_i(x, t, y)$  for the second-order PDE in Eqn. (1).

Governing equation	$a_1$	$a_2$	$a_3$	$a_4$	$a_5$
Transient heat conduction	0	1	$\alpha(x)$	0	0
Transient convection diffusion	0	1	$1/Re$	$v$	0
Acoustic wave propagation	$Ma^2$	0	1	0	0

### B. Spatio-Temporal Discretization

The governing Eqn. (1) is solved on the unit space-time interval. The domain is discretized by  $N_p + 2$  equidistantly spaced points  $x_k : k \in [0, N_p + 1]$  and  $N_t + 1$  equidistant time instants  $t^l : l \in [0, N_t]$ . The step size designation is  $\Delta x$  and  $\Delta t$ . Following our previous contribution [23], we distinguish between interior points, where Eqn. (1) is evaluated, and boundary (ghost) points ( $x_0, x_{N_p+1}$ ) which are used to implement the boundary conditions. The reader is referred to Ref. [23] for a detailed description of combinations of Dirichlet or Neumann boundary conditions.

### C. Spatial Optimization Problem

To formulate the optimization problem, we need a time-discrete initial formulation, cf. [23]. In the present paper, temporal derivatives are approximated by the following exemplary backward Finite Difference (FD) formulae:

$$\frac{\partial y}{\partial t} = \frac{y^l - y^{l-1}}{\Delta t} + \mathcal{O}(\Delta t), \quad \frac{\partial^2 y}{\partial t^2} = \frac{y^l - 2y^{l-1} + y^{l-2}}{\Delta t^2} + \mathcal{O}(\Delta t). \tag{2}$$

Introducing Eqn. (2) into Eqn. (1), we obtain the semi-discrete residual form

$$R(x, t^l) = -\frac{\partial}{\partial x} \left( a_3 \frac{\partial y}{\partial x} \right) + a_4 \frac{\partial y}{\partial x} + y^l \left( a_5 + \frac{a_1}{\Delta t^2} + \frac{a_2}{\Delta t} \right) - \left[ a_1 \left( \frac{2y^{l-1} - y^{l-2}}{\Delta t^2} \right) + a_2 \frac{y^{l-1}}{\Delta t} + f \right] = 0. \tag{3}$$

The desired weighted residual form of Eqn. (3) is obtained by

$$\int_{\Omega} z(x, t^l) R(x, t^l) dx = 0. \quad (4)$$

The choice of the weighting function  $z$  offers many options. Using  $z = R(x, t^l)$ , the optimization problem resembles the *Bubnov-Galerkin* approach with a Least-Square-like cost function. While this formulation permits, e.g., maintaining a quadratic cost function as outlined in Ref. [25], the disadvantage is the larger number of terms in the cost function due to the binomial form and the required modeling of quadratic terms with quantum circuits. We therefore opt for a *Ritz-Galerkin* approach with  $z = y(x, t^l)$ , which yields smaller quantum circuits and less cost function contributions. The related solution to Eqn. (4), i.e.,

$$\underbrace{\int_{\Omega} y^l \left[ \left( a_5 + \frac{a_1}{\Delta t^2} + \frac{a_2}{\Delta t} \right) y^l - \frac{\partial}{\partial x} \left( a_3 \frac{\partial y^l}{\partial x} \right) \right] dx}_{B(y^l, y^l)} + \underbrace{\int_{\Omega} y^l \left[ a_4 \frac{\partial y^{l-1}}{\partial x} - \left[ a_1 \left( \frac{2y^{l-1} - y^{l-2}}{\Delta t^2} \right) + a_2 \frac{y^{l-1}}{\Delta t} + f \right] \right] dx}_{F(y^l)} = 0, \quad (5)$$

is equivalent to the solution of the variational problem [27], [28] characterized by an objective function  $J$  that consists of a bilinear term  $B$  and a linear term  $F$ , viz.

$$\min_{y^l} J(y^l) \quad \text{with} \quad J(y^l) := B(y^l, y^l) - 2F(y^l). \quad (6)$$

The residual form in Eqn. (3) must be adapted to the requirements of Eqn. (6), i.e.,  $B$  needs to be positive semi-definite and symmetric, and numerical schemes are therefore usually limited to symmetric or skew-symmetric approaches [19], [25]. To avoid this limitation, we are motivated to treat the convective term associated with  $a_4$  explicitly and to classify it in  $F$  in Eqn. (5). Due to the explicit treatment, the stability of the numerical method constrains the time step size in terms of a *Courant* number criterion, i.e.,  $\Delta t \leq \Delta x/v$  [29].

To obtain a discrete formulation, approximations for both, the spatial integrals and the spatial derivatives in Eqn. (5), must be introduced. Spatial integrals are approximated using the second-order accurate midpoint rule, cf. [23]. The approximation of spatial derivatives is linked to the design of the quantum circuits and is presented in Section III.

### III. QUANTUM MODEL

The quantum model describes how FD operations with  $y$  can be represented using the principles of quantum computing. In Sections III-A and III-B, we first discuss the encoding of the state  $y$  in a quantum register and subsequently introduce the hybrid quantum-classical framework for realizing the VQA. The evaluation, viz. the measurement, of individual qubits is, due to statistical influences, fairly demanding on a QC. To reduce the number of measurements, the strategy pursued here is based on two different circuits, one representing the bilinear term  $B$  and one for the linear term  $F$  in Eqn. (6). In both cases, the discrete integral is determined over

all points of the inner region at a measuring qubit (ancilla), instead of measuring the individual contributions for each qubit. Finally, the fundamental building blocks for the representation of inhomogeneous material properties and upwind biased differential operators with Quantum-Nonlinear-Processing-Units (QNPU) are introduced in Sec. III-C.

#### A. State Encoding

We encode the state amplitudes in a quantum register comprising  $n = \log_2(N_p)$  qubits that span an orthonormal basis in the complex Hilbert space by the tensor product of each qubit's subspace. The  $i$ -th element of the basis is given in the binary representation  $\text{bin}(i)$  as  $|\text{bin}(i)\rangle = \mathbf{e}_i$ , e.g., for the *little-endian* convention  $\mathbf{e}_{i=0} = |0\rangle \otimes |0\rangle \otimes \dots \otimes |0\rangle$  or  $\mathbf{e}_{i=1} = |0\rangle \otimes |0\rangle \otimes \dots \otimes |1\rangle$ , using the *Dirac* notation for the base vectors  $|0\rangle = (1, 0)^\top$  and  $|1\rangle = (0, 1)^\top$  of each individual qubit [30].

The physical state  $y$  is represented variably by the control vector  $\mathbf{v}^l \in \mathbb{R}^{c+1}$ ,  $\mathbf{v}^l := (\lambda_0^l, \boldsymbol{\lambda}_c^l)^\top$  ( $c \in \mathbb{N}$ ) and realized by the time-dependent ansatz

$$y(x, t^l, \mathbf{v}^l) = \lambda_0^l u(x, t^l, \boldsymbol{\lambda}_c^l). \quad (7)$$

Due to the probabilistic nature of quantum states, one needs to enforce the *partition of unity* constraint in the  $L^2$  scalar product of the ansatz function  $u$  [31], [32], viz.  $(u^*, u)_{L^2} = 1$ . Here, the asterisk represents the complex conjugate of the quantum states, and the factor  $\lambda_0^l$  is introduced to account for general solutions not only norm-preserving ones. This enables the discrete representation of  $u(x, t^l, \boldsymbol{\lambda}_c^l)$ , viz. vector  $\mathbf{u}$ , by the amplitudes  $u_k$  of the quantum state  $|u\rangle$  in the quantum register as  $\mathbf{u} = \sum_k u_k \mathbf{e}_k = |u\rangle$  (known as *amplitude encoding*). Mind that, contrary to real-valued physical states  $y$ , quantum amplitudes  $u_k$  include phase information and thus employ a complex notation, and that the quantum register is in the following restricted to the interior points, viz.

$$\mathbf{u}^l = u_0^l \mathbf{e}_0 + \underbrace{\sum_{k=1}^{N_p} u_k^l \mathbf{e}_k}_{\text{register}} + u_{N_p+1}^l \mathbf{e}_{N_p+1}. \quad (8)$$

#### B. Hybrid Classical-Quantum Approach

For each time step  $l$ , the VQA approach minimizes the discretized cost function (6), by adjusting the control parameters  $\mathbf{v}^l := (\lambda_0^l, \boldsymbol{\lambda}_c^l)^\top$  that shape the ansatz  $\lambda_0^l \mathbf{u}$ . This quantum state  $|u\rangle$  results from the parameterized quantum gate  $U(\boldsymbol{\lambda}_c^l)$  applied to  $|0\rangle$ .

The optimization is executed on a hybrid classical-QC hardware, as indicated in Fig. 1. On the right-hand side of Fig. 1, quantum registers are used to evaluate the cost function  $J$  on the QC. At the same time, the classical computer updates the control  $\mathbf{v}_i$ , within an optimization procedure as depicted on the left-hand side of Fig. 1. As outlined in the introduction to this Section, only a single evaluation is used in order to mitigate the measurement problem on QCs [33], [34]. Therefore, both quantum circuits representing the bilinear and linear

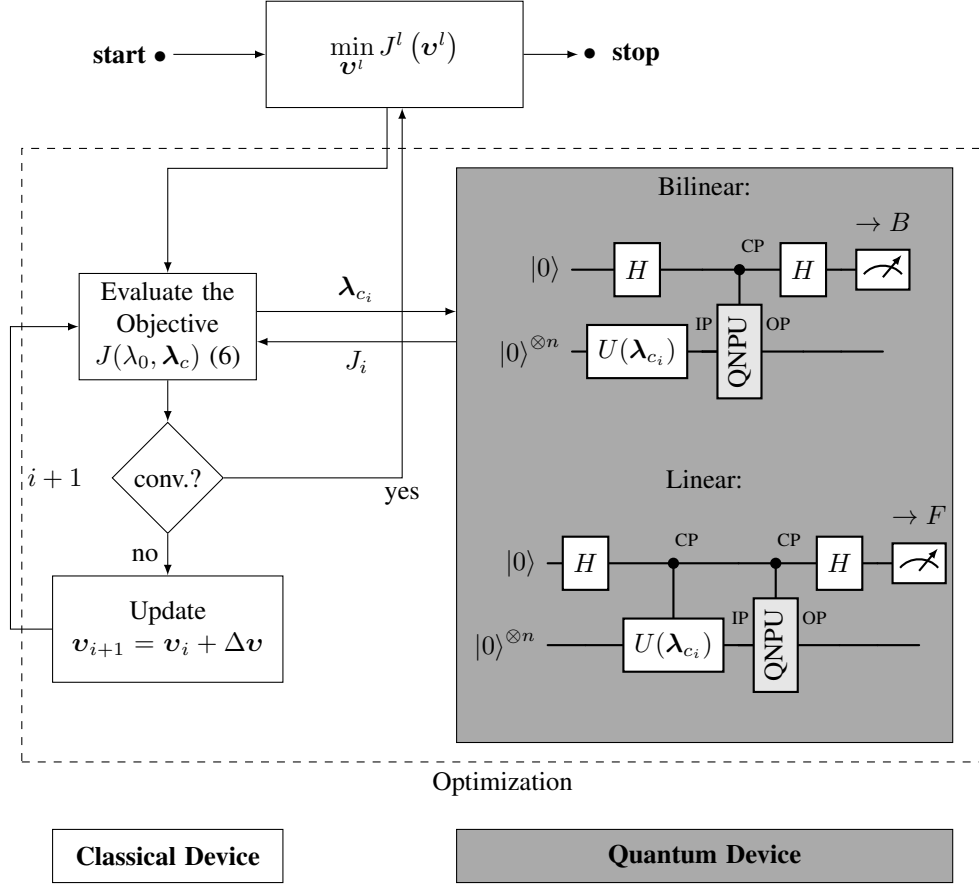


Fig. 1: Sketch of the hybrid classical-QC optimization in the VQA. The bilinear and linear circuit on the right-hand side show, the Hadamard gate  $H$ , the ansatz gate  $U(\lambda_c^l)$ , the QNPU module, and the measurement gauge on the ancilla. The abbreviation CP marks a control port while IP & OP denote input/output ports, respectively.

integrals, on the right-hand side of Fig. 1, are based on the Hadamard test [30] with an upper measurement qubit (ancilla) and the lower working qubits, all initialized to the base state  $|0\rangle$ . The only difference between the two circuits of Fig. 1 is the ancilla-controlled ansatz gate  $U(\lambda_c^l)$  (bottom circuit), which corresponds to the overlap operation (i.e., a scalar product) required in the linear term  $F(y)$ .

For the sake of completeness, the employed parameterization  $U(\lambda_c^l)$  of the quantum state  $|u\rangle$  should also be mentioned here. It is based on a hardware-efficient bricklayer topology [35] and supports arbitrary ansatz types with variable depth to increase the expressibility of the solution space, cf. [23].

### C. Building Blocks for Physical Modeling with QNPUs

The QNPU block in Fig. 1 indicates the section where the physical modeling takes place. To this end, each summand in  $J$ , given in Eqn. (5), is translated into quantum gates by an individual QNPU. Similarly, boundary conditions also contribute to  $J$  through their particular QNPUs, and the interested reader is again referred to Over et al. [23] for details.

Prior to discussing the models of the individual spatial discretization schemes with quantum gates in the Sec. IV, we explain the building blocks required for this task. The description opens with the external contributions of a potential field  $p(x_k, t^l)$ , e.g., used to represent inhomogeneous material properties, followed by the so-called adder circuits to compose FD expressions, and finalizes with the overlap operation for source-term contributions. To motivate the three building blocks below, we refer to the example of a simple first-order FD approximation for the expression  $y_k a_k \partial y_k / \partial x \sim y_k a_k (y_{k+1} - y_k) / \Delta x$  which involves products between unknowns at the same  $(k, k)$  and at different locations  $(k, k + 1)$ .

1) *The Potential Term:*  $p(x_k, t^l)$  models contributions of the general form  $\sum_{k=1}^{N_p} [\lambda_0^2 u_k^* p_k u_k]^l$ . With reference to Eqn. (5) this obviously involves parts of the nonlinear term  $B(y^l, y^l)$  evaluated for the current time step, i.e.,  $\int y^l (a_5 + \frac{a_1}{\Delta t^2} + \frac{a_2}{\Delta t}) y^l dx$ . Depending on the employed spatial discretization with an FD scheme, the potential term also includes a contribution from the diffusive term  $\int y^l \frac{\partial}{\partial x} (a_3 \frac{\partial y^l}{\partial x}) dx$ . Moreover, the nonlinear convective term  $\int y^l a_4 (\frac{\partial y^{l-1}}{\partial x}) dx$  also contributes to  $p$  for an explicit treatment of the flux coefficient  $a_4 = y^{l-1}$  as it is also indicated in Fig. 5.

The corresponding QNPU circuit is assembled by  $n$  Toffoli gates and  $n$  additional auxiliary qubits because the product  $u_k^* p_k u_k$  is non-unitary [36], see Fig. 2. Note that a potential function  $p$  must also be represented by a series of quantum gates. For non-constant functions, the same ansatz gate  $U(\bar{\lambda}_c)$  is employed for encoding  $p$ , subject to an additional optimization problem to achieve the trained control vector

$$\bar{\lambda}_c = \min_{\lambda_c} (1 - \lambda_0 \langle u(\lambda_c) | p \rangle) \quad \text{with} \quad \frac{1}{\lambda_0^2} = \sum_1^{N_p} p_k^* p_k. \quad (9)$$

To differentiate the ansatz of a potential  $p$ ,  $P(\bar{\lambda}_c)$  indicates the application of the trained parameters  $\bar{\lambda}_c$  to  $U(\bar{\lambda}_c)$ . Multiple potentials can be staggered to create higher-order point-wise products, as required for nonlinearities [25].

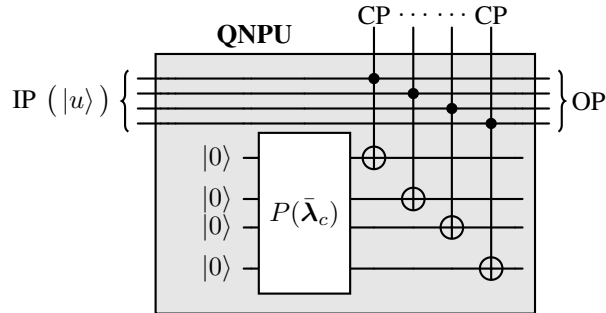


Fig. 2: QNPU schematic for the potential contribution  $P$ , e.g., for  $n = 4$  qubits. The ansatz gate for encoding  $p$  is indicated with  $P(\bar{\lambda}_c)$ , where  $\bar{\lambda}_c$  are the trained parameters. Indicated are the QNPU's control ports with CP, the input ports with IP, and the output ports with OP.

2) *The Adder Circuits:* are used to perform classical bit shift operations [30], [37] required for products of shifted locations, e.g.,  $u_k^* u_{k+1}^l$  or  $u_k^* u_{k-1}^l$ . The adder circuit is the building block to include any FD stencil



in the weighted residual approach forming the cost function  $J$ . Adder circuits are key for the reduction of the gate complexity, see Sec. IV-E. For the example of a weighted integration of a forward differentiation scheme  $y \partial y / \partial x \sim y_k (y_{k+1} - y_k)$  the adder circuit performs (shift-down) [25],

$$\sum_{k=1}^{N_p} u_k |\text{bin}(k-1)\rangle \rightarrow \sum_{k=1}^{N_p} u_{k+1} |\text{bin}(k-1)\rangle. \quad (10)$$

A half-adder circuit with one CNOT and one Toffoli gate is applicable for  $n = 2$  qubits [30]. In the case of  $n > 2$ , the additional  $(n - 2)$  carry (auxiliary) qubits lead to a full-adder circuit with  $n - 2$  CNOTs and  $2n - 2$  Toffoli gates. Figure 3 depicts the corresponding QNPU circuits for  $n = 4$  qubits.

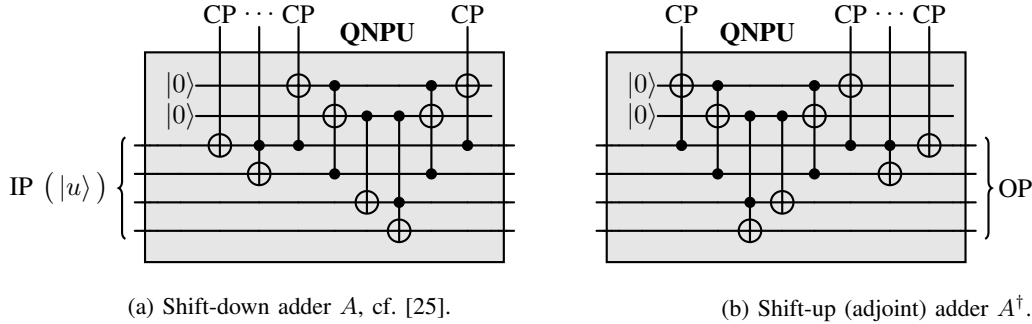


Fig. 3: QNPU schematic for the adder (shift) circuits, e.g., for  $n = 4$  qubits. The control ports are indicated with CP, the input ports with IP, and the output ports with OP.

Two adder circuits are required, i.e., one for assessing the upper diagonals, e.g., for a forward differencing scheme, and one for assessing the lower diagonals, e.g., for a backward differencing scheme. The adder circuit  $A$  displayed in Fig. 3a performs a shift-down operation (forward differencing) and its conjugate-transpose  $A^\dagger$  in Fig. 3b performs a shift-up (backward differencing) instead. Furthermore, multiple shift-up or shift-down operations can be stacked sequentially by applying the circuit  $q$  times. This provides the possibility of representing arbitrary FD stencils, as detailed in Sec. IV. Mind that the number of involved gates can be reduced by using multi-controlled gates, being native on particular hardware [38]. For further discussion, the reader is referred to the Section on complexity in Ref. [23].

3) *The Source Term:* contribution  $\int y f dx$  to  $J$  in Eqn. (5) is represented as an overlap operation (scalar product) on a QC. Therefore, the linear term in Fig. 1 has a "controlled"  $U(\lambda_{c_i})$  gate in contrast to the bilinear term. This circuit is used to realize products such as  $u_k^{*l} u_k^{l-1}$ , where the QNPU is realized with the trained approach  $U^\dagger(\lambda^{l-1})$ .

All three fundamental building blocks described above, i.e., potential, adder, and source QNPU, can be combined to model discretized transport operators. For example, the combination of potential and shift QNPU is used to implement an advective contribution to the objective functional, i.e.,  $\int y a_4 \left(\frac{\partial y}{\partial x}\right) dx$ . This combination is illustrated in Fig. 4. Herein, the potential  $P(\bar{\lambda}_c)$  is trained to represent the coefficient distribution  $a_4$ .

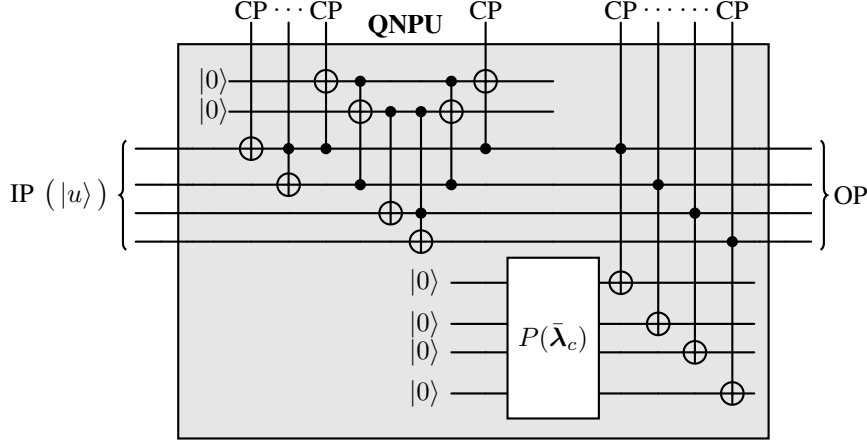


Fig. 4: Schematic for the adder-potential QNPU  $A_p$  for the example of  $n = 4$  qubits. The ansatz gate for the potential  $p$  is indicated by  $P(\bar{\lambda}_c)$ . The abbreviations CP, IP, OP mark the control, input, and output ports, respectively.

Figure 5 depicts a QNPU implementation of a nonlinear convective contribution to the objective functional, i.e.,  $\int y^l a_4^{l-1} \left( \frac{\partial y^{l-1}}{\partial x} \right) dx$ , by the combination of two potentials (Fig. 2), one shift (Fig. 3), and one source term. To build the convective term following an explicit treatment, the coefficient is  $a_4^{l-1} = p y^{l-1}$  and thus the old control variable  $\lambda_c^{l-1}$  is used for  $U^\dagger(\lambda_c^{l-1})$  in Fig. 5. The trained ansatz  $P(\bar{\lambda}_c)$  represents a potential  $p$ , which can be used to imply a point-wise modulation of the coefficient, e.g., being zero or one. The adder as depicted here, implements a forward FD approximation and can be modified easily to implement other (higher-order) FD approximations. The QNPU is subsequently realized in combination with another  $U^\dagger(\lambda_c^{l-1})$ , substituted in the source term, cf. Sec. III-C3, to prepare the state  $a_4^{l-1} \left( \frac{\partial y^{l-1}}{\partial x} \right)$ . The assembled QNPU in Fig. 5 is used in the bottom circuit on the right-hand side of Fig. 1, which in turn is multiplied with the current state to get the final cost function contribution, i.e.  $\int y^l [\dots] dx$ .

#### IV. QUANTUM COMPUTATIONAL FLUID DYNAMICS

The current Section illustrates the conceptual process for translating FD stencils into the quantum framework. Due to the amplitude encoding strategy, i.e., Eqn. (8), its application is limited to a collocated variable arrangement and global ansatz functions. The technique is first demonstrated for elementary FD stencils (Sec. IV-A) and subsequently generalized in Sec. IV-B. Thereafter, we employ the general strategy for modeling an inhomogeneous thermal diffusivity (Sec. IV-C) as well as for higher-order convection schemes (Sec. IV-D). The Section closes with an analysis of the associated gate complexities in Sec. IV-E.

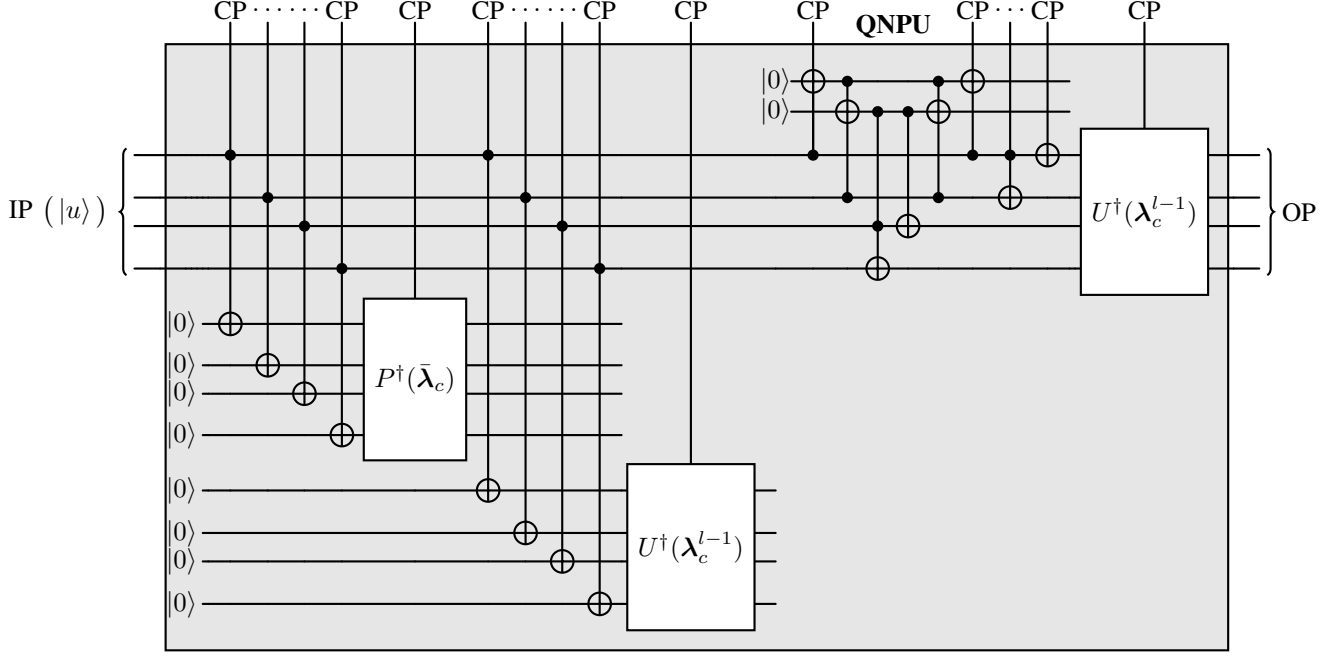


Fig. 5: QNPU schematic of adder-potential-potential  $A^{\dagger}_{p^{\dagger}p^{\dagger}}$  with the ansatz  $U^{\dagger}(\lambda_c^{l-1})$  for the example of  $n = 4$  qubits. The ansatz gates to mimic a convective coefficient  $a_4$  are the potential  $p$ , indicated with  $P^{\dagger}(\bar{\lambda}_c)$ , and the ansatz gate  $U^{\dagger}(\lambda_c^{l-1})$  (nonlinearity). The subsequent gate  $U^{\dagger}(\lambda_c^{l-1})$  represents the previous  $l - 1$  (explicit scheme) time step. The abbreviations CP, IP, OP mark the control, input, and output ports, respectively.

### A. Elementary FD Schemes

Using a midpoint integration rule, the discrete cost function contributions for approximating first derivatives by elementary FD formulae on an equidistant mesh follow from

$$\text{1st-order forward:} \quad J_{\text{forw-1}} = \int_{\Omega} y \frac{\partial y}{\partial x} dx = \sum_k y_k (y_{k+1} - y_k), \quad (11)$$

$$\text{1st-order backward:} \quad J_{\text{back-1}} = \int_{\Omega} y \frac{\partial y}{\partial x} dx = \sum_k y_k (y_k - y_{k-1}), \quad (12)$$

$$\text{2nd-order central:} \quad J_{\text{cent-1}} = \int_{\Omega} y \frac{\partial y}{\partial x} dx = \frac{1}{2} \sum_k y_k (y_{k+1} - y_{k-1}). \quad (13)$$

Similarly, the approximate FD contribution that involves a second derivative is of

$$\text{2nd-order central:} \quad J_{\text{cent-2}} = \int_{\Omega} y \frac{\partial^2 y}{\partial x^2} dx = \frac{1}{\Delta x} \sum_k y_k (y_{k+1} - 2y_k + y_{k-1}). \quad (14)$$

Substituting the quantum ansatz of Eqns. (7, 8) into the Eqns. (11,12), the cost function contributions read

$$J_{\text{forw-1}} = \lambda_0^2 \left( \sum_k u_k^*(\lambda_c) u_{k+1}(\lambda_c) - 1 \right), \quad (15)$$

$$J_{\text{back-1}} = \lambda_0^2 \left( 1 - \sum_k u_k^*(\lambda_c) u_{k-1}(\lambda_c) \right). \quad (16)$$

The QNPU of Fig. 3 applies  $A$  to implement  $\sum_k u_k^*(\lambda_c) u_{k+1}(\lambda_c)$  for the forward differencing, while the

backward difference term,  $\sum_k u_k^*(\lambda_c)u_{k-1}(\lambda_c)$ , is modeled by  $A^\dagger$  instead.

Analogous to classical FD, the quantum implementation of the central difference in Eqn. (13) can be expressed by the averaging of forward (11) and backward (12) stencils. However, when introduced to the weighted residual method, the result vanishes for a periodic case, since the sums of the forward (15) and backward (16) differences neutralize, i.e.,  $J_{\text{cent-1}}$  does not contribute to  $J$ . Similarly, the CDS approximation of the second derivative  $J_{\text{cent-2}}$ , could be expressed as  $J_{\text{cent-2}} = (J_{\text{for-1}} - J_{\text{back-1}})/\Delta x$ . The approximation results in a symmetric tridiagonal matrix, which is represented by the adder circuit of Fig. 3 and can be efficiently executed on a QC [23], [25]. In a periodic case, the difference of the two sums agrees with twice its components and the cost function contribution simplifies to

$$J_{\text{cent-2}} = +2/(\Delta x)J_{\text{for-1}} = -2/(\Delta x)J_{\text{back-1}}. \quad (17)$$

### B. Diagonal operations with QNPUs

We now generalize the formalism of Sec. IV-A to the diagonals of band matrices, which typically occur for FD approximations of transport equations on Cartesian grids. Since the implementation of non-periodic boundary conditions is already covered in Ref. [23] and will not be repeated here, we again restrict the derivation to periodic boundaries.

The notation of a band matrix  $C$ , with bandwidth  $b_w$ , obtained from an FD discretization reads  $C = c_{kj} e_k \otimes e_j$ . A vector representation of the band matrix's  $q$ -th non-zero diagonal, where  $q \in [-\lfloor (b_w - 1)/2 \rfloor, +\lfloor (b_w - 1)/2 \rfloor]$  ( $\lfloor \dots \rfloor$  - integer operation), is written as  $\mathbf{p}_q = p_{qk} e_k = c_{\underline{k}(j+q)} \delta_{\underline{k}j} e_k$ . Here,  $\delta_{\underline{k}j}$  denotes the unit tensor where the underline marks a non-contractable index. The operation selects the respective  $q$ -th diagonal through the index  $(j + q)$  when contracted by the dot product. Thus,  $q = 0$  points to the main diagonal, and  $q > 0$  or  $q < 0$  denotes the  $q$ -th super- or subdiagonals, respectively. Note that all diagonals are of the same length in a periodic setting. The action of the matrix  $C$  on the cost function  $J$  is separated into (non-zero) diagonal contributions as

$$\sum_o^{\min(q), \max(q)} J_o = \sum_k y_k p_{o_k} y_{(k+|o|)} \Delta x. \quad (18)$$

In an analogy to the variable potential term  $p$ , cf. Sec. III-C1 and Eqn. (9), the ansatz gate  $U(\lambda_c)$  is trained to reproduce the non-constant  $q$ -th diagonal of  $C$  by solving an overlap problem before its use in the corresponding QNPU. The normalization conditions for the description of a vector on a QC need to apply for each non-zero diagonal of the band matrix  $C$ . For this purpose, the scaling factor  $\tilde{\lambda}_q$ , which corresponds to the factor  $\lambda_0^l$  in Eqn. (7), is introduced. As a result, the vector of the  $q$ -th diagonal  $\mathbf{p}_q$  is encoded by  $\tilde{\lambda}_q \tilde{\mathbf{p}}_q$ . In the case of Toeplitz matrices, i.e., constant diagonal entries, the representation of the diagonal by the ansatz  $U(\lambda_c)$  can be expressed, up to normalization, by Hadamard gates, avoiding the solution of the optimization problem of Eqn. (9).

The contribution of the main diagonal ( $q = 0$ ) to the cost function of Eqn. (18) is formed by the normalized diagonal entries, with the state  $\tilde{p}_0$ . The evaluation for this diagonal is conducted by the circuit of Fig. 2 and reads

$$J_0 = \lambda_0^2 \sum_k u_k^* \underbrace{\tilde{\lambda}_0 \tilde{p}_{0k}}_{p_{0k} = c_{kk}} u_k \Delta x. \quad (19)$$

In case  $c_{kk} \equiv \text{const.}$ , the circuit evaluation is unnecessary, and the cost function contribution results in  $J_0/\Delta x = \lambda_0^2 \tilde{\lambda}_0$ , e.g.,  $\lambda_0^2 c_{00}$ . For the off-diagonals  $|q| \geq 1$ , the same formalism is implemented, with the diagonals represented by a quantum state. Here, the QNPU in Fig. 4 is applied, with the adder operator appearing  $q$  times. As an example, the cost function contributions for  $q = \pm 1$  are

$$J_1 = \lambda_0^2 \tilde{\lambda}_1 \sum_k u_k^* \tilde{p}_{1k} A u_k \Delta x, \quad J_{-1} = \lambda_0^2 \tilde{\lambda}_{-1} \sum_k u_k^* \tilde{p}_{-1k} A^\dagger u_k \Delta x, \quad (20)$$

where the conjugate-transpose  $A^\dagger$  performs a shift-up instead of a shift-down, cf. Sec. III-C. Although the presented approach is applicable to every matrix, it is most suitable for symmetric matrices because the off-diagonal entries are identical for the same  $|q| \geq 1$ , and the cost function contributions for  $q < 0$  can be dropped by doubling the contributions of  $q > 0$ . Applying this to the cost function contributions for  $q = \pm 1$  yields

$$J_1 + J_{-1} = 2\lambda_0^2 \tilde{\lambda}_1 \sum_k u_k^* \tilde{p}_{1k} A u_k \Delta x. \quad (21)$$

Note, that Eqn. (21) is a generalization of the discussion in Sec. IV-A. As a last remark, it is important to highlight, that training a quantum state allows to introduce boundary conditions by manipulating the corresponding entries in  $\tilde{p}_q$ .

### C. Non-constant Diffusivity

Inhomogeneous material properties, such as a spatially variable thermal diffusivity  $\alpha(x)$ , frequently occur in engineering applications. To illustrate the related quantum model, a periodic diffusion operator in a weighted residual formulation is considered, cf. Eqn. (5),

$$\int_{\Omega} y(x) \frac{\partial}{\partial x} \left( \alpha(x) \frac{\partial}{\partial x} y(x, t) \right) dx. \quad (22)$$

The derivatives in Eqn. (22) are approximated by a consecutive application of backward (outer) and forward (inner) FDs, resulting in the following FD matrix for the interior points

$$\begin{aligned}
& \frac{1}{\Delta x^2} \underbrace{\begin{bmatrix} 1 & 0 & \dots & -1 \\ -1 & 1 & \dots & 0 \\ & \ddots & \ddots & \\ 0 & \dots & -1 & 1 \end{bmatrix}}_{\text{backward (outer) FD}} \begin{bmatrix} \alpha_1 & 0 & \dots & 0 \\ 0 & \alpha_2 & \dots & 0 \\ & & \ddots & \\ 0 & \dots & 0 & \alpha_{N_p} \end{bmatrix} \underbrace{\begin{bmatrix} -1 & 1 & \dots & 0 \\ & -1 & 1 & \\ & & \ddots & \ddots \\ 1 & \dots & 0 & -1 \end{bmatrix}}_{\text{forward (inner) FD}} \begin{bmatrix} y_1 \\ y_2 \\ \vdots \\ y_{N_p} \end{bmatrix} \\
& = \frac{1}{\Delta x^2} \begin{bmatrix} -(\alpha_{N_p} + \alpha_1) & \alpha_1 & \dots & \alpha_{N_p} \\ \alpha_1 & -(\alpha_1 + \alpha_2) & \alpha_2 & 0 \\ & \ddots & \ddots & \ddots \\ \alpha_{N_p} & \dots & \alpha_{N_p-1} & -(\alpha_{N_p-1} + \alpha_{N_p}) \end{bmatrix} \begin{bmatrix} y_1 \\ y_2 \\ \vdots \\ y_{N_p} \end{bmatrix} \approx \frac{\partial}{\partial x} \left( \alpha(x) \frac{\partial}{\partial x} y(x, t) \right). \tag{23}
\end{aligned}$$

From Eqn. (23), it is evident that a symmetric band matrix is obtained. As elaborated in Sec. IV, this allows modeling the dynamics using only  $\lfloor b_w/2 \rfloor + 1 = 2$  quantum circuits. This observation is confirmed by forming the discretized expression of Eqn. (22), which reads

$$J_\alpha = \frac{1}{\Delta x^2} \left( \sum_k y_k \underbrace{(-\alpha_k - \alpha_{k-1})}_{\text{diagonal}} y_k + 2 \sum_k y_k \underbrace{\alpha_k}_{\substack{\text{super-} \\ \text{sub-} \\ \text{diagonal}}} y_{k+1} \right) \Delta x. \tag{24}$$

To show the similarity with the general framework presented in Eqns. (19-20), we define  $c_{kk} = (\alpha_k + \alpha_{k-1}) = \tilde{\lambda}_0 \tilde{p}_{0k}$  and  $c_{k(j+1)} = c_{k(j-1)} = \alpha_k = \tilde{\lambda}_1 \tilde{p}_{1k}$ . The resulting cost function contribution for the quantum model reads

$$J_\alpha = \frac{1}{\Delta x^2} (J_0 + 2J_1) = \frac{1}{\Delta x} \left( \lambda_0^2 \tilde{\lambda}_0 \sum_k u_k^* \tilde{p}_{0k} u_k + 2\lambda_0^2 \tilde{\lambda}_1 \sum_k u_k^* \tilde{p}_{1k} A u_k \right). \tag{25}$$

#### D. Convective Kinematics

Convective transport is subject to velocity-induced transport ( $v = y$ ) in Eqn. (5), i.e.,

$$\int_{\Omega} y \left( y \frac{\partial y}{\partial x} \right) dx. \tag{26}$$

To treat the convective term, a first-order UDS or higher-order upwind biased schemes [29], [39], [40] are commonly used. The particular higher-order schemes considered here refer to CDS, LUDS, and QUICK scheme [41], where the CDS is of course not upwind biased. Knowledge about the flow direction is mandatory to apply upwind biased approximations. Classically, the UDS scheme follows from a max-operation as given for the discretized approximation of the weighted residual formulation in Eqn. (26), viz.

$$J_{\text{UDS}} = \sum_k \left( \max[y_k, 0] \underbrace{y_k (y_k - y_{k-1})}_{\text{Eqn. (12)}} - \max[-y_k, 0] \underbrace{y_k (y_{k+1} - y_k)}_{\text{Eqn. (11)}} \right). \tag{27}$$

In the quantum model, the max operation is substituted by the discrete mask functions  $\mathbf{m}^+$ ,  $\mathbf{m}^-$ , whose entries are either 0 or 1 depending on the flow direction. Here the superscript (+) indicates a positive and the superscript (-) a negative flow direction along the coordinate axis. Mind that the mask function entries are linearly dependent, i.e.,  $m_k^+ = 1 - m_k^-$ . The application of  $\mathbf{m}^+$  and  $\mathbf{m}^-$  to the velocity  $y_k$  is performed by a point-wise multiplication ( $\max[y_k, 0] = m_k^+ y_k$ ) and ( $\max[-y_k, 0] = -m_k^- y_k$ ), realized with the circuit outlined in Fig. 2. The underbraced terms in Eqn. (27) are identical to the backward and forward differencing expressions discussed in Sec. IV-A.

Given an arbitrary one-dimensional periodic flow field, the weak formulation of the UDS as a matrix-vector multiplication reads equivalent to the inhomogeneous material treatment in Sec. IV-C as

$$\begin{aligned}
& \begin{bmatrix} y_1 \\ y_2 \\ \vdots \\ y_{N_p} \end{bmatrix}^T \begin{bmatrix} m_1^+ & & & \\ & m_2^+ & & \\ & & \ddots & \\ & & & m_{N_p}^+ \end{bmatrix} \begin{bmatrix} y_1 \\ y_2 \\ \vdots \\ y_{N_p} \end{bmatrix} \begin{bmatrix} 1 & 0 & \dots & -1 \\ -1 & 1 & \dots & 0 \\ & \ddots & \ddots & \\ 0 & \dots & -1 & 1 \end{bmatrix} \begin{bmatrix} y_1 \\ y_2 \\ \vdots \\ y_{N_p} \end{bmatrix} \\
& - \begin{bmatrix} y_1 \\ y_2 \\ \vdots \\ y_{N_p} \end{bmatrix}^T \begin{bmatrix} -m_1^- & & & \\ & -m_2^- & & \\ & & \ddots & \\ & & & -m_{N_p}^- \end{bmatrix} \begin{bmatrix} y_1 \\ y_2 \\ \vdots \\ y_{N_p} \end{bmatrix} \begin{bmatrix} -1 & 1 & \dots & 0 \\ & -1 & 1 & \\ & & \ddots & \ddots \\ 1 & \dots & 0 & -1 \end{bmatrix} \begin{bmatrix} y_1 \\ y_2 \\ \vdots \\ y_{N_p} \end{bmatrix} \\
& = \begin{bmatrix} y_1 \\ y_2 \\ \vdots \\ y_{N_p} \end{bmatrix}^T \begin{bmatrix} -m_1^- y_1 + m_1^+ y_1 & m_1^- y_1 & \dots & -m_1^+ y_1 \\ -m_2^+ y_2 & -m_2^- y_2 + m_2^+ y_2 & m_2^- y_2 & \\ & \ddots & \ddots & \ddots \\ m_{N_p}^- y_{N_p} & \dots & -m_{N_p}^+ y_{N_p} & -m_{N_p}^- y_{N_p} + m_{N_p}^+ y_{N_p} \end{bmatrix} \begin{bmatrix} y_1 \\ y_2 \\ \vdots \\ y_{N_p} \end{bmatrix}. \tag{28}
\end{aligned}$$

The corresponding discrete weighted residual expression of the band matrix with non-constant diagonals in Eqn. (28) is

$$J_{\text{UDS}} = \left( \sum_k y_k \underbrace{(-m_k^- + m_k^+) y_k}_{\text{diagonal}} y_k - \sum_k y_k \underbrace{m_k^+ y_k}_{\text{sub-diagonal}} y_{k-1} + \sum_k y_k \underbrace{m_k^- y_k}_{\text{super-diagonal}} y_{k+1} \right), \tag{29}$$

where  $(-m_k^- + m_k^+) y_k$  simplifies to  $|y_k|$ . The products of  $y_k$  and  $m_k^{+/-}$  which arise along the off-diagonals, require using the circuit introduced in Fig. 5, i.e.,  $a_4 = y_k m_k^{+/-}$ .

The method's trade-off is the previous knowledge of  $\mathbf{y}$  to construct the mask parameters  $\mathbf{m}^-$ ,  $\mathbf{m}^+$  that are required for the quantum circuits evaluation. For a passive scalar transport, the advection velocity is known a priori but in a general nonlinear convection problem, the extraction of the velocity directions is a challenging task for the QC. To overcome a QC operation creating the mask function, an explicit time stepping is a viable option. The required quantum encoding of a previous velocity again uses the encoding denoted in Eqn. (7) and requires a training approach similar to Eqn. (9).

Higher-order methods are derived by extending the information to more remote neighboring points. For the sake of clarity, the following discussion is restricted to a velocity in the positive coordinate direction. The central location  $k$  in the finite approximation is referred to as  $C$ . The related upstream location is depicted by  $U \leftarrow k-1$ , while the downstream location refers to  $D \leftarrow k+1$ . To increase the order of the FD approximation, information from a second (remote) upstream location is required, i.e.,  $UU \leftarrow k-2$ . The strategy introduced for the UDS can be extended by exchanging the approximation of the derivative  $\partial y/\partial x|_C$  in Eqn. (27) with

$$\frac{y_C - y_U}{\Delta x} + \mathcal{O}(\Delta x) \quad \rightarrow \quad \text{UDS}, \quad (30)$$

$$\frac{y_D - y_U}{2\Delta x} + \mathcal{O}(\Delta x^2) \quad \rightarrow \quad \text{CDS}, \quad (31)$$

$$\frac{3y_C - 4y_U + y_{UU}}{2\Delta x} + \mathcal{O}(\Delta x^2) \quad \rightarrow \quad \text{LU DS}, \quad (32)$$

$$\frac{2y_D + 3y_C - 6y_U + y_{UU}}{6\Delta x} + \mathcal{O}(\Delta x^3) \quad \rightarrow \quad \text{QUICK}. \quad (33)$$

Obviously, the matrix bandwidth  $b_w$  increases for the higher-order schemes in comparison to the UDS example in Eqn. (28) ( $b_w = 3$ ). While the symmetric CDS remains compact ( $b_w = 3$ ), the LUDS results in a bandwidth of  $b_w = 5$  and the QUICK [41] stencil recovers a larger band of  $b_w = 7$ . The implementation applies the ideas presented in Sec. IV-A. The shifted indices, e.g.,  $k-1$ , are realized analog to Eqns. (15-16) by using the shift operation. Similarly, a sequence of two adders is used to realize a  $k \pm 2$  shift. Again, we use a mask function as outlined in Eqn. (27). The cost function contributions for the above-mentioned schemes for positive/negative velocities read

$$J_{\text{UDS}} = \underbrace{\lambda_0^2 \tilde{\lambda}_0}_{\lambda_0^3} \sum_k u_k^* \underbrace{\tilde{p}_{k_0}}_{|u_k|} u_k - \lambda_0^2 \sum_k u_k^* \underbrace{\tilde{\lambda}_{-1} \tilde{p}_{-1k}}_{m_k^+ y_k} A^\dagger u_k + \lambda_0^2 \sum_k u_k^* \underbrace{\tilde{\lambda}_1 \tilde{p}_{1k}}_{m_k^- y_k} A u_k, \quad (34)$$

$$\begin{aligned} 2 J_{\text{CDS}} = & -\lambda_0^2 \sum_k u_k^* \underbrace{\tilde{\lambda}_{-1} \tilde{p}_{-1k}}_{m_k^+ y_k} A^\dagger u_k + \lambda_0^2 \sum_k u_k^* \underbrace{\tilde{\lambda}_1 \tilde{p}_{1k}}_{m_k^+ y_k} A u_k \\ & + \lambda_0^2 \sum_k u_k^* \underbrace{\tilde{\lambda}_{-1} \tilde{p}_{-1k}}_{m_k^- y_k} A^\dagger u_k - \lambda_0^2 \sum_k u_k^* \underbrace{\tilde{\lambda}_1 \tilde{p}_{1k}}_{m_k^- y_k} A u_k, \end{aligned} \quad (35)$$

$$\begin{aligned} 2 J_{\text{LU DS}} = & 3 \underbrace{\lambda_0^2 \tilde{\lambda}_0}_{\lambda_0^3} \sum_k u_k^* \underbrace{\tilde{p}_{0k}}_{|u_k|} u_k \\ & - 4 \lambda_0^2 \sum_k u_k^* \underbrace{\tilde{\lambda}_{-1} \tilde{p}_{-1k}}_{m_k^+ y_k} A^\dagger u_k + \lambda_0^2 \sum_k u_k^* \underbrace{\tilde{\lambda}_{-2} \tilde{p}_{-2k}}_{m_k^+ y_k} A^{\dagger 2} u_k \\ & + 4 \lambda_0^2 \sum_k u_k^* \underbrace{\tilde{\lambda}_1 \tilde{p}_{1k}}_{m_k^- y_k} A u_k - \lambda_0^2 \sum_k u_k^* \underbrace{\tilde{\lambda}_2 \tilde{p}_{2k}}_{m_k^- y_k} A^2 u_k, \end{aligned} \quad (36)$$



$$\begin{aligned}
6 J_{\text{QUICK}} = & 3 \underbrace{\lambda_0^2 \tilde{\lambda}_0}_{\lambda_0^3} \sum_k u_k^* \underbrace{\tilde{p}_{0k}}_{|u_k|} u_k \\
& + 2\lambda_0^2 \sum_k u_k^* \underbrace{\tilde{\lambda}_1 \tilde{p}_{1k}}_{m_k^+ y_k} A u_k - 6\lambda_0^2 \sum_k u_k^* \underbrace{\tilde{\lambda}_{-1} \tilde{p}_{-1k}}_{m_k^+ y_k} A^\dagger u_k + \lambda_0^2 \sum_k u_k^* \underbrace{\tilde{\lambda}_{-2} \tilde{p}_{-2k}}_{m_k^+ y_k} A^{\dagger 2} u_k \\
& - 2\lambda_0^2 \sum_k u_k^* \underbrace{\tilde{\lambda}_{-1} \tilde{p}_{-1k}}_{m_k^- y_k} A^\dagger u_k + 6\lambda_0^2 \sum_k u_k^* \underbrace{\tilde{\lambda}_1 \tilde{p}_{1k}}_{m_k^- y_k} A u_k - \lambda_0^2 \sum_k u_k^* \underbrace{\tilde{\lambda}_2 \tilde{p}_{2k}}_{m_k^- y_k} A^2 u_k.
\end{aligned} \tag{37}$$

In the case of a passive scalar transport, the main diagonal contribution becomes associated with the prescribed transport velocity  $v$  ( $p_{0k} \rightarrow |v_k|$ ) and the mask-function product simplifies as  $m_k^{+/-}|y_k| \rightarrow m_k^{+/-}|v_k|$ , which is inherently known. Nevertheless, all non-symmetric operators have to be treated explicitly, cf. Sec. II. It is worth mentioning that CDS is independent of the flow direction by definition. Therefore, a reformulation of the cost function to  $2 J_{\text{CDS}} = (\sum_k y_k y_k y_{k+1} - \sum_k y_k y_k y_{k-1})$ , without mask functions, is preferred to reduce computational cost.

### E. Gate Complexity

The decoherence time defines the interval in which a qubit remains stable before losing its quantum state due to interactions with the environment [42]. This time interval is generally short for current QCs, suggesting to limit the number of required quantum operations [43] by using shallow quantum circuits. To analyze the gate scalability of the proposed method, the number of gates is evaluated in terms of single-qubit ( $R_z, R_y, U, \dots$ ) and two-qubit (CNOT, ...) gates, for all presented QCFD circuits of Sec. III. Mind that the gate complexity study only assesses the QNPU gates, states like the mask functions  $m^{+/-}$  for the matrix contributions in  $p_q$  are assumed to be realized efficiently by an appropriate ansatz.

Figure 6 provides the results of the gate complexity study. Therein, the building blocks of Sec. III, cf.  $P$  Fig. 2 and  $A$  Fig. 3, are marked by  $\triangle$  &  $\square$ , respectively, while the lines correspond to the matrix's diagonals, e.g.,  $q \in \{1, 2\}$ .

The building block QNPU are independent of the derivative matrix structure, allowing to reproduce any band matrix with excellent gate complexities, as it is shown by the evolution of the symbols in Fig. 6. In particular, the main diagonal complexity is based on the *polylog* scaling,  $\mathcal{O}(\log(n)^r) : r \in \mathbb{R}$ , of the potential circuit  $P$ . Similarly, the off-diagonals benefit from the same *polylog* complexity of the adder circuit  $A$  and the potential  $P$ . It is also evident that the scaling is independent of the bandwidth  $b_w$ , which encourages the application for higher-order approximation schemes. In conclusion, a generic band matrix is implemented with *polylog* complexity by the proposed algorithm. To guarantee this scaling w.r.t. the number of qubits, the efficient amplitude encoding by a suitable ansatz is essential [12], [16], [44]–[47].

## V. NUMERICAL RESULTS

The Section verifies VQA results against results obtained from a classical approach for three different problems, i.e., heat transfer, Burgers' equation, and wave equation. The first two Subsections of the results are

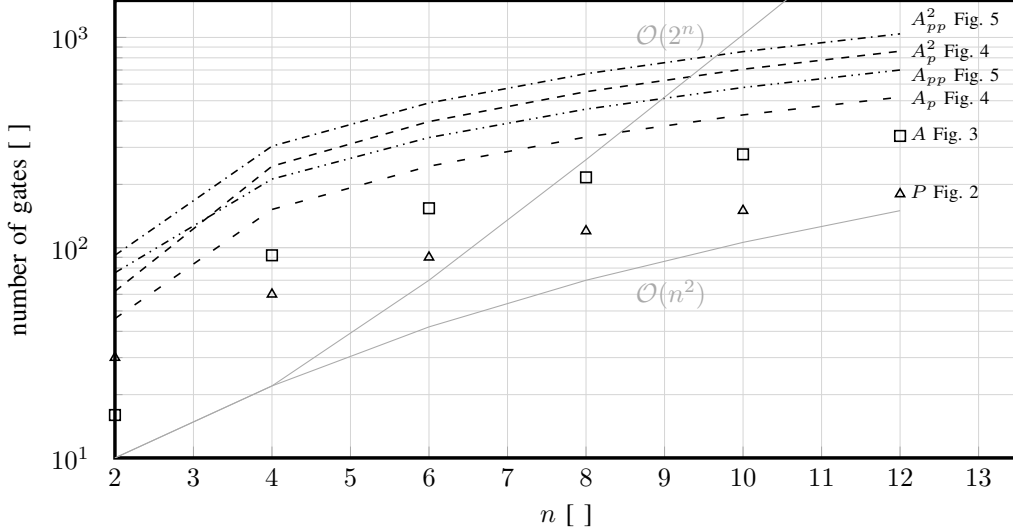


Fig. 6: Gate complexity of the employed QNPU assemblies in Sec. III-C.

dedicated to heat transfer simulations using the example of transient heat conduction with inhomogeneous diffusivity (Sec. V-C) and steady advective/conductive heat transfer at two different *Péclet* numbers, i.e.,  $Pe_{\Delta x} = 0.3$  and 30 (Sec. V-D). Subsequently, the nonlinear momentum transfer is studied for the inviscid case ( $Re \rightarrow \infty$ , Sec. V-E) and a viscous case at  $Re = 100$  (Sec. V-F). Finally, Sec. V-G reports results for the wave equation. Depending on the properties of the quadratic cost function contribution  $B$  in Eqn. (5), either implicit or (iterative) explicit approaches are employed, as discussed in Sec. II. The source term contribution  $f$  in Eqn. (1) is not the subject of this work and is therefore not considered in the applications. An extension to include this contribution is possible, as shown in Ref. [23].

The study is based on the previously described FD approximations, which were used both for the classical simulation and for the development of the analogue QNPU employed by the VQA. Deviations between the VQA result and the classical result are assessed using the  $l_2$ -error and the trace distance error

$$\varepsilon_{l_2} = \sqrt{\sum_k (y_k^{\text{FD}} - y_k^{\text{VQA}})^2}, \quad \varepsilon_{\text{tr}} = \sqrt{\left(1 - \left| \sum_k \frac{y_k^{\text{FD}}}{\|\mathbf{y}^{\text{FD}}\|_2} \frac{y_k^{\text{VQA}}}{\|\mathbf{y}^{\text{VQA}}\|_2} \right|^2 \right)}. \quad (38)$$

#### A. VQA Approach

For the sake of simplicity, the employed parameterization  $U(\boldsymbol{\lambda}_c^l)$  of the quantum state  $|u\rangle = U(\boldsymbol{\lambda}_c^l)|0\rangle$  are restricted to the hardware-efficient fixed-structure ansatz, suggested by Bravo et al. [18], assembled in brick-layered structure of depth  $d \in [4, 9]$  [25]. In general lower depth circuits are preferred to limit the computational effort. However, higher error levels might motivate to increase the depth and simultaneously reduce the amount of qubits to reduce the computational resources for this study.

We would like to point out again that we assume a periodic basic pattern of all matrices as a starting point. In this regard, the implementation of non-periodic boundary conditions takes place in two steps [23]. First, inherently periodic contributions of the QNPU along the boundaries are neutralized by a correction of the objective

functional called  $J_{\text{DN}}$ . The objective functional is subsequently modified a second time to take into account the respective Dirichlet or Neumann contributions. For the QNPU's of the convective kinematics, boundary conditions could also be enforced by manipulating the mask function.

In line with Ref. [23], transient influences are represented by cost function contributions to potential  $J_{\text{P}}$  and source  $J_{\text{S}}$  terms.

Measurement of the quantum states neglect noise errors and simplify the procedure to the trace-out of the ancilla qubit [30]. The corresponding density matrix  $\rho_{\text{ancilla}}$  is recovered by a single shot of the state vector simulation.

### B. Optimization Strategy

The gradient-based optimization of the ansatz gate  $U(\boldsymbol{\lambda}_c^l)$  employs a version of the established BFGS approach [48]. The strategy is also used for optimizing the quantum encoding of flow fields, e.g. the previous time velocity, cf. Eqn. (9). The derivative of the cost function is approximated by the *Parameter Shift Rule* [49]–[51], which enables the reuse of quantum circuits. The optimal parameters  $\boldsymbol{v}^{l-1}$  of the previous time iteration serve as the first estimate for the next time step. The convergence of the optimizer is judged by the  $l_2$ -norm of the derivative with respect to a defined tolerance, i.e.,  $\text{tol} > \|\nabla J(\boldsymbol{v}^l)\|_2$ .

### C. Transient Heat Conduction with Non-Uniform Diffusivity

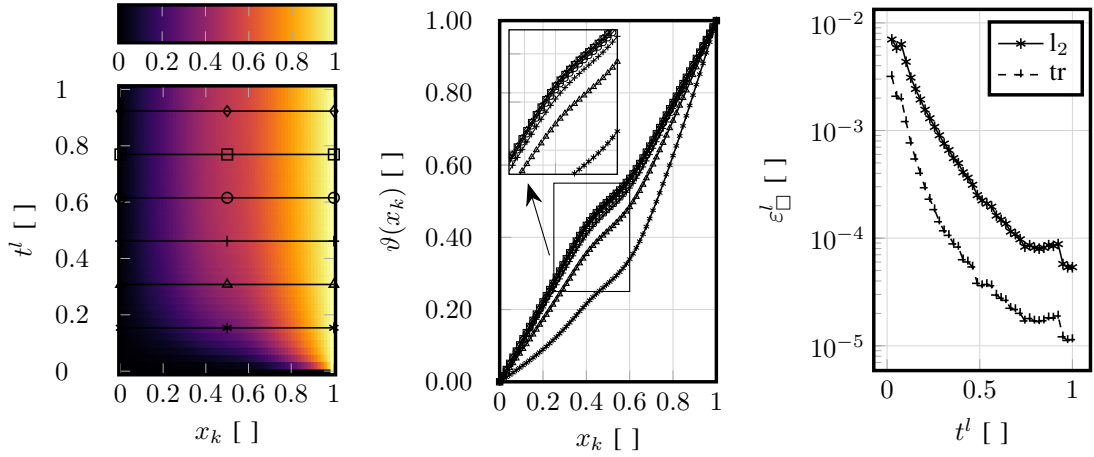
The first application refers to the transient heat conduction ( $a_1 = 0, a_2 = 1$ ). It observes the evolution of the dimensionless temperature  $y = \vartheta(x, t)$  for an inhomogeneous material with non-constant thermal diffusivity  $a_3 = \alpha(x)$ , neglecting convective heat transport and source terms ( $a_4 = a_5 = f = 0$ ). Dirichlet boundary conditions are employed at both ends of the domain, with  $\vartheta|_{x=0} = 0$  and  $\vartheta|_{x=1} = 1$ , and the temperature is initialized with  $\vartheta(x, t = 0) = 0$ . The VQA simulations are conducted with a circuit depth of  $d = 9$ , using  $n = 6$  qubits, i.e.,  $N_{\text{p}} = 64$  interior grid points. The convergence criterion of the optimizer is set to  $\text{tol} = 10^{-3}$ , limited to a maximum number of 400 iterations per time step.

The thermal diffusivity  $\alpha(x)$  follows a Gaussian distribution and reaches a maximum in the center of the domain, viz.  $\alpha(x) = 1 + \exp(-100(0.5 - x)^2)$ . The spatially varying heat flux is captured by the contributions  $p_{0_k} = -\alpha_{k-1} - \alpha_k$  and  $p_{1_k} = \alpha_k$  as indicated in Eqn. (23). Combining the cost function contributions of Sec. IV with the contributions of the boundary conditions to  $J_{\text{P}}$ ,  $J_{\text{S}}$  and the boundary specific contribution  $J_{\text{DN}}$  as introduced in Ref. [23], the optimization problem to be solved per time step reads

$$\min_{\boldsymbol{v}} J(\boldsymbol{v}), \text{ where } J(\boldsymbol{v}) = \underbrace{-J_0 - 2J_1}_{-J_{\alpha}(25)} + \underbrace{J_{\text{DN}_{\alpha}} + J_{\text{S}}}_{\text{b.c. influenced [23]}} + J_{\text{P}}. \quad (39)$$

As mentioned above, the two-step implementation of the boundary conditions [23], initially neutralizes the inherently periodic contributions of the QNPU's along the boundaries by  $J_{\text{DN}_{\alpha}}$  and subsequently introduces contributions of the inhomogeneous Dirichlet condition at  $x = 1$  to the source term contribution  $J_{\text{S}}$ .

Figure 7 illustrates results obtained for the VQA and the classical FD approach. The spatio/temporal evolution of the VQA-predicted temperature  $\vartheta(x, t)$  for  $N_t + 1 = 40$  time steps is displayed in Fig. 7a, where the abscissa refers to the spatial location and the ordinate to the time. The Figure also indicates the six time instants that are used to compare spatial temperature profiles obtained from the VQA and the classical method in Fig. 7b. Figure 7c shows the temporal evolution of the two error measures introduced in Eqn. (38). An excellent predictive agreement between VQA and FD methods is indicated by Fig. 7b. The inclination of the steady state profiles is halved in the center of the domain due to the doubling of the diffusivity. Moreover, both the  $l_2$ -error and the trace distance decrease to values below  $10^{-4}$  as the system approaches the steady-state solution with temporal averages of  $\bar{\varepsilon}_{l_2} = 1.1 \cdot 10^{-3}$  and  $\bar{\varepsilon}_{tr} = 3.1 \cdot 10^{-4}$ , cf. Fig. 7c. The results demonstrate that the proposed quantum model for non-homogeneous material properties can accurately reproduce classical simulation results.



(a) VQA predicted temperature evolution. Lines and symbols mark time instants assessed in Subfig. (b). (b) Spatial temperature profiles computed by the VQA (lines) and an FD method (symbols) for the six time instants given in Subfig. (a). (c) Temporal evolution of the error measures  $\varepsilon_{l_2}$  and  $\varepsilon_{tr}$ .

Fig. 7: Comparison of VQA and FD results for the transient heat conduction problem with non-constant diffusivity. Results refer to  $N_p = 64$  interior grid points and  $N_t + 1 = 40$  time steps, using Dirichlet conditions ( $\vartheta|_0 = 0$ ,  $\vartheta|_1 = 1$ ) and an initially zero temperature ( $\vartheta(x, t = 0) = 0$ ).

#### D. Steady Advection-Diffusion

The second case covers the steady ( $a_1 = a_2 = 0$ ), source-free ( $f = a_5 = 0$ ) advection-diffusion problem. The application describes the spatial temperature distribution  $y = \vartheta(x)$  of a fluid that is advected with a constant positive velocity  $a_4 = v$ . Diffusive transport is based on a constant thermal diffusivity  $a_3 = \alpha = 1$ , and the problem is subject to Dirichlet conditions at both ends of the domain, viz.  $\vartheta|_{x=0} = \vartheta_0 = 0$  and  $\vartheta|_{x=1} = \vartheta_1 = 1$ . In this case, Eqn. (1) reduces to an ODE with the analytical solution

$$\hat{\vartheta}(x) = \vartheta_0 + \frac{e^{Pe_{\Delta x} x/L} - 1}{e^{Pe_{\Delta x}} - 1}(\vartheta_1 - \vartheta_0), \quad (40)$$

where the *Péclet* number  $Pe_{\Delta x} = \Delta x v / \alpha$  describes the ratio between convective and diffusive transport. Hence, the VQA implementation can be verified against the classical approach and also validated against the analytical solution (40).

The problem is discretized with  $N_p = 16$  interior grid points with  $n = 4$  qubits and a circuit depth of  $d = 4$ . The convergence criterion of the optimization is set to  $\text{tol} = 10^{-8}$ , limited to a maximum number of 300 iterations. The steady-state problem is iterated to convergence, achieved within  $\mathcal{O}(10)$  iterations depending on  $Pe_{\Delta x}$  and maintaining a reduction of the initial residual by  $10^{-6}$ . For a prescribed constant velocity  $v$ , the convective term in Eqn. (1) linearizes, such that the main diagonal contribution  $p_{0_k}$  simplifies to  $|v_k|$  and the off-diagonal contributions read  $m_k^{+/-}|v_k|$ , cf. Sec. IV-D. As in the previous case, the cost function employs contributions from the boundary condition by means of  $J_{\text{DN}}$  and  $J_S$  [23] in addition to the diffusion  $J_{\text{cent-2}}$  and the (explicit) contributions for the convective kinematics  $J_C$ , viz.

$$\min_{\mathbf{v}} J(\mathbf{v}), \text{ where } J(\mathbf{v}) = -a_3 \overbrace{J_{\text{cent-2}}}^{(17)} + a_4 \overbrace{J_C}^{(34-37)} + J_P + \underbrace{a_3 J_{\text{DN}_{\text{cent-2}}} - a_4 J_{\text{DN}_C} + J_S}_{\text{b.c. influenced [23]}}. \quad (41)$$

The advective contributions  $J_C$  and  $J_{\text{DN}_C}$  take  $C = \{\text{UDS, CDS, LUDS, QUICK}\}$  and adjust to the chosen advection scheme as introduced in Eqns. (34-37). The correction of the symmetric 2nd-order central difference approximation at the boundaries  $J_{\text{DN}_{\text{cent-2}}}$  agrees for the left and right end of the domain. The correction, labeled  $J_{\text{DN}_C}$ , of the periodic convective contribution  $J_C$  is implemented similarly. Again, the inhomogeneous Dirichlet condition at  $x = 1$  induces a contribution to the source term contribution  $J_S$ . The solution is iterated to convergence by means of iterating the  $J_P$  and  $J_S$  contributions.

The test case serves to assess the performance of the convective schemes presented in Sec. IV-D. For this purpose, simulations are conducted for two different *Péclet* numbers, i.e.,  $Pe_{\Delta x} = 0.3$  and  $Pe_{\Delta x} = 30$ . Figure 8 and Tab. II display the predictive performance of the VQA implementations in comparison to the results obtained by the classical method and analytical solutions, the latter is indicated by a red line.

When attention is directed to the diffusion dominated smaller *Péclet* number as in Fig. 8a, all convection schemes deliver accurate results, with minor exceptions for the UDS, which displays a noticeable degree of numerical diffusion. As expected, the higher order CDS, LUDS and QUICK convection methods yield very good agreement with the analytical solution. For all investigated convective approximations, the predictive agreement of the VQA results and the classical results is very good, which is also seen by the values in Tab. II. Despite these accurate  $l_2$  results in Tab. II, the trace-distance results indicate that the employed ansatz offers room for improvement w.r.t. the distinguishability.

For the advection dominated larger *Péclet* number, the influence of the convective approximation becomes more pronounced, as given in Fig. 8b. As expected, results of the unbiased CDS scheme reveal instabilities due to lack of dominance of the main diagonal and the sign change of the secondary diagonals given by the stencil. The instabilities are seen for both classical and VQA results, though the agreement between them is

naturally less exact, cf. Tab. II. The discrepancy between the classical and the VQA is smaller for the three upwind-biased schemes in comparison to CDS, which is also reflected in the  $\varepsilon_{l_2}$  and  $\varepsilon_{tr}$  values. The results for the non-monotonic QUICK scheme displayed in Fig. 8b suffer from issues at the right end, whereas the schemes that avoid downwind influences, i.e., LUDS and UDS, provide more accurate results. The differences for the VQA and the classical method at the right end of the domain when using the QUICK scheme are due to monotonicity issues.

Monotonicity problems of higher-order convective schemes are usually addressed by additional TVD or NVD corrections [52], which limit the higher-order contributions to preserve monotonicity. However, such corrections usually involve further unfavorable min / max operations in the QC framework. Based on these findings, the following two Subsections are restricted to the UDS scheme for the investigation of the nonlinear Burgers' equation in Sec. V-E, and Sec. V-F.

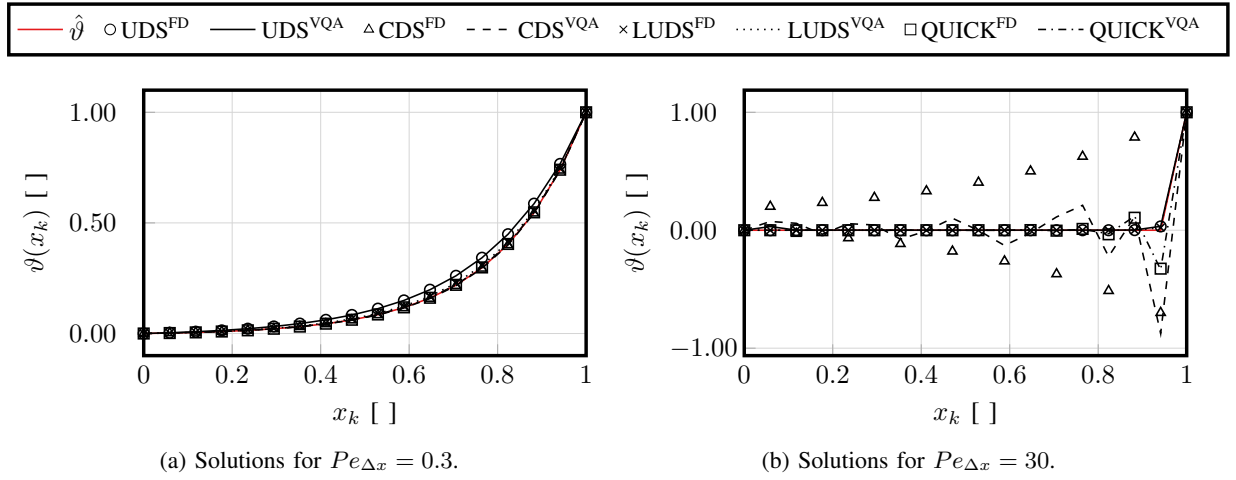


Fig. 8: Results for the steady advection-diffusion problem obtained from the VQA (lines) and the FD (symbols) methods in comparison to the analytical solution (red-line) (40) on a grid with  $N_p = 16$  interior points for two different local *Péclet* numbers  $Pe_{\Delta x}$ .

TABLE II: Deviations of VQA and FD-results in the  $l_2$ -norm ( $\varepsilon_{l_2}$ ) and trace distance ( $\varepsilon_{tr}$ ) obtained for the steady advection-diffusion problem depicted in Fig. 8.

Convection scheme	$l_2$ -norm $\varepsilon_{l_2}$		trace distance $\varepsilon_{tr}$	
<i>Péclet</i> Number	$Pe = 0.3$	$Pe = 30$	$Pe = 0.3$	$Pe = 30$
UDS $\mathcal{O}(\Delta x)$	$2.21 \times 10^{-5}$	$3.14 \times 10^{-2}$	$8.58 \times 10^{-1}$	$5.59 \times 10^{-2}$
CDS $\mathcal{O}(\Delta x^2)$	$2.00 \times 10^{-5}$	$1.33 \times 10^0$	$8.38 \times 10^{-1}$	$8.96 \times 10^{-1}$
LUDS $\mathcal{O}(\Delta x^2)$	$3.22 \times 10^{-5}$	$4.15 \times 10^{-4}$	$8.44 \times 10^{-1}$	$3.08 \times 10^{-2}$
QUICK $\mathcal{O}(\Delta x^3)$	$3.98 \times 10^{-5}$	$1.62 \times 10^{-2}$	$8.40 \times 10^{-1}$	$4.44 \times 10^{-1}$

### E. Inviscid Nonlinear Convective Transport

The third application focuses on the unsteady ( $a_1 = 0, a_2 = 1$ ), inviscid ( $a_3 = 0$ ), nonlinear convection  $a_4 = y = v$  problem with  $a_5 = f = 0$ . The left boundary is assigned to a Dirichlet inflow condition  $v|_{x=0} = 2$

and the right boundary is assigned to a Neumann outflow condition  $\partial v / \partial x|_{x=1} = 0$ . The latter is approximated by a first-order FD approximation, viz.  $(v_{N_p} - v_{N_p-1}) / \Delta x = 0$ . The employed initial velocity field features a discontinuity (shock wave) and reads

$$v(x, t = 0) := \begin{cases} 2 & : x \leq 0.5, \\ 1 & : x > 0.5. \end{cases} \quad (42)$$

Simulations employ the UDS scheme (34) throughout  $N_t + 1 = 30$  time step on  $N_p = 16$  interior grid points for  $n = 4$  qubits with a constant *Courant* number of  $v|_{x=0} \Delta t / \Delta x = 0.6$ . The VQA ansatz employs a circuit depth of  $d = 4$  and the convergence criterion of the optimization is set to  $\text{tol} = 10^{-7}$ , limited to a maximum iteration number of 300. The optimization is advanced explicitly in time for a sequence of  $l$  time steps that minimize

$$\min_{\mathbf{v}} J(\mathbf{v}), \text{ where } J(\mathbf{v}) = a_4 \overbrace{J_{\text{UDS}}^{(34)}} - \underbrace{J_{\text{DN}_{\text{UDS}}} + J_{\text{S}} + J_{\text{P}}}_{\text{b.c. influenced [23]}}. \quad (43)$$

Periodic boundary contributions of the UDS scheme are corrected by  $J_{\text{DN}_{\text{UDS}}}$ , as discussed in Ref. [23], and non-zero Dirichlet boundary values are introduced through an additional contribution to the source term  $J_{\text{S}}$ , whereas such term does not occur on the right end for the combination of UDS and positive velocities.

Figure 9 illustrates results obtained for the VQA and the classical FD approach. The spatio/temporal evolution of the VQA predicted velocity is displayed in Fig. 9a with the abscissa indicating the spatial location and the ordinate the time. The six time instants to compare the spatial velocity profiles obtained from the VQA and the classical method are marked in Fig. 9a. Figure 9c shows the temporal evolution of the two error measures introduced in Eqn. (38). Analyzing the results, the use of the diffusive first-order upwind scheme reveals no instabilities across the shock and the predictive agreement between the classical and the VQA results is again excellent, as indicated by Fig. 9b. This very good agreement between VQA and classical solution is confirmed by the  $l_2$ -error and trace error depicted in Fig. 9c. As long as the shock has not reach the right boundary both error measures maintain a very low level of  $\varepsilon_{l_2}^l < 10^{-4}$  and  $\varepsilon_{\text{tr}}^l < 10^{-3}$ , respectively. However,  $\varepsilon_{l_2}$  and  $\varepsilon_{\text{tr}}$  increase towards the end of the simulation time, due to the velocity gradient  $\partial v / \partial x$  vanishing as the shock leaves the domain around  $t = 0.7$ .

#### F. Viscous Nonlinear Convective Transport (Burgers' Equation)

The fourth test case adds viscous forces to the previous nonlinear momentum ( $a_4 = \gamma = \nu$ ) transport ( $a_1 = a_5 = f = 0, a_2 = 1$ ). To this end, the *Reynolds* number is set to  $Re = 100$  ( $a_3 = 0.01$ ). The investigated example is subjected to periodic boundary conditions  $v|_{x=0} = v|_{x=1}$  and initialized with a Gaussian distribution in the domain's spatial second quarter, viz.  $v(x, t = 0) = 1 \cdot \exp(-(10x - 3.5)^4)$ . The spatial discretization employs  $N_p = 64$  interior grid points or  $n = 6$  qubits, and the simulation evolves over  $N_t + 1 = 5$  time steps

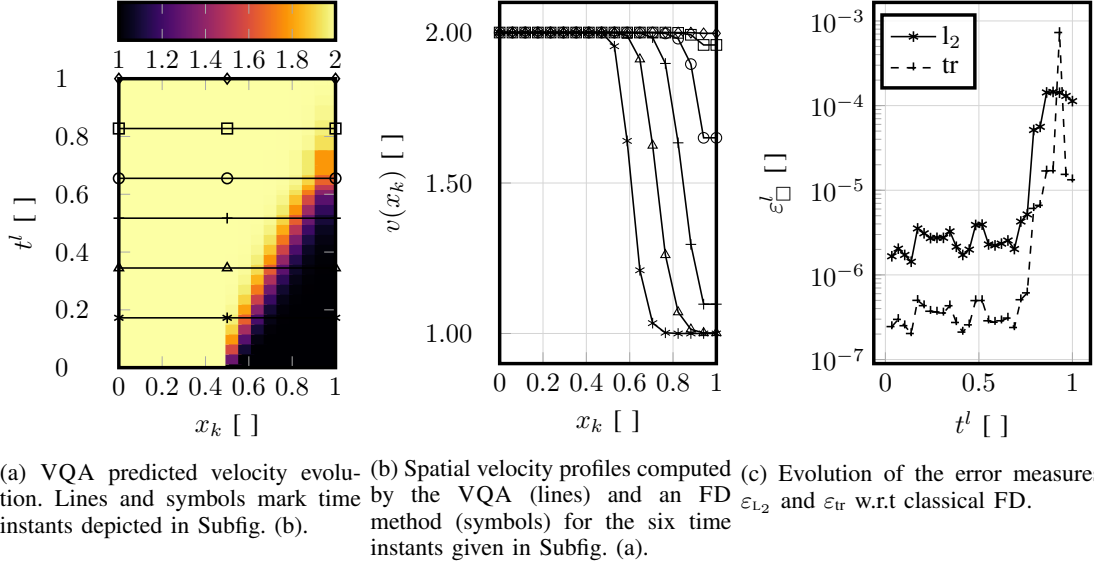


Fig. 9: Results for the inviscid nonlinear convection of a shock wave obtained from the VQA and FD method when using a first-order UDS on a grid with  $N_p = 16$  interior points.

with a constant *Courant* number of  $1 \cdot \Delta t / \Delta x = 1$ . Each time instant requires solving the optimization problem

$$\min_{\mathbf{v}} J(\mathbf{v}), \text{ where } J(\mathbf{v}) = -a_3 \overbrace{J_{\text{cent-2}}^{(17)}} + a_4 \overbrace{J_{\text{UDS}}^{(34)}} + J_P + J_S. \quad (44)$$

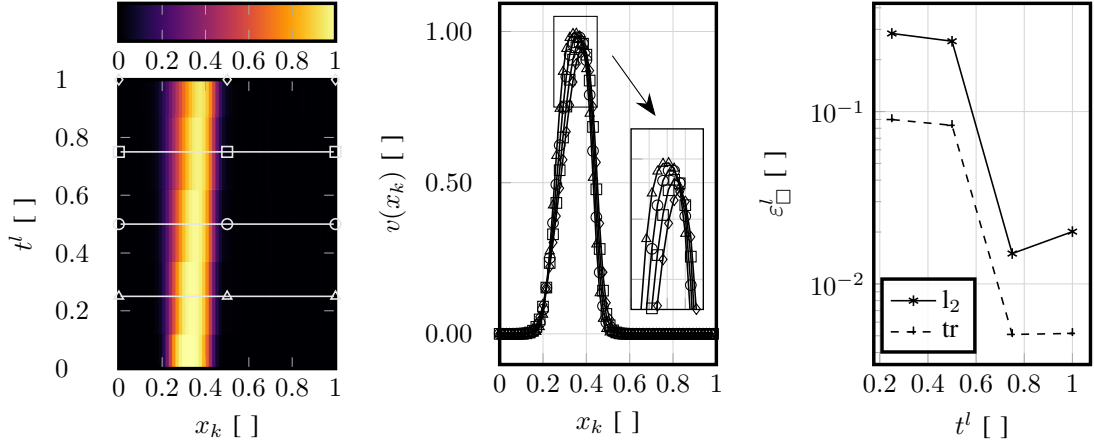
Due to the periodic setting, no corrections are needed to compensate periodic diffusive and convective boundary terms. Diffusive and transient terms are treated implicitly, such that the contributions  $J_P$  and  $J_S$  only account for the parts of the temporal discretization and the convective term as described in Sec. III. The VQA ansatz employs a circuit depth of  $d = 7$  and the convergence criterion of the optimization is  $\text{tol} = 10^{-7}$ , limited to a maximum iteration number of 300.

The comparison between the VQA and the FD results is displayed in Fig. 10 which is decomposed into the same arrangement of Subfigures as Fig. 9 of the previous Subsection, i.e. space/time VQA results, velocity profiles comparisons, and temporal evolution of the error measures.

The nonlinear transport of the initial Gaussian distribution increasingly reveals a velocity-induced stretching on the downstream front and a steeper gradient on the upstream front, cf. Fig. 10a. The UDS approximation additionally supports a broader downstream front, by introducing additional diffusion as it is elaborated in Sec. V-D. The tilting of the initially uniform peak into a triangle shape indicates a successful mapping of the nonlinear convective kinematics, which is also confirmed by the velocity profiles in Fig. 10b. Here the center of area evolves in positive flow-direction. The VQA and FD results not only agree visually but also the error measures (Eqn. (38)) depicted in Fig. 10c decrease with successive time steps and indicate a good agreement. Despite the positive overall trend, the accuracy at the initial time step is low due to the fix number of iterations. In the case of a nearly constant velocity profile, the additional inner-iterations in subsequent time steps would improve the accuracy, since it is naturally easier to converge starting from a better initial guess. This effect



can be observed in Fig. 10c. The time averaged  $l_2$ -error falls below  $2 \times 10^{-1}$  and the trace-distance reduces to  $5.9 \times 10^{-2}$ .



(a) VQA simulations with lines and (b) Velocity profiles recovered by symbols marking equidistant time the VQA (lines) and FD-reference profiles for comparison in Subfig. (b). (symbols) for the four time instants indicated in Subfig. (a). (c) Evolution of the error measures  $\epsilon_{l_2}$  and  $\epsilon_{tr}$  w.r.t classical FD.

Fig. 10: Temporal evolution of the VQA results for the nonlinear transport problem governed by the Burgers' equation at  $Re = 100$  on a  $N_p = 64$  interior grid points subject to periodic boundary conditions, for  $N_t + 1 = 5$  time steps, and initialized to a Gaussian distribution  $v(x, t = 0) = \exp(-(10x - 3.5)^4)$ .

### G. Linear Wave Equation

The final application addresses the transport of pressure perturbations  $y = p$  governed by the linear wave equation ( $a_1 = Ma^2$ ,  $a_3 = 1$ , and  $a_2 = a_4 = a_5 = f = 0$ ). In this investigation, the *Mach* number is set to  $Ma^2 = 1$ , both boundaries are modeled as reflective walls by the Dirichlet conditions  $p|_{x=0} = p|_{x=1} = 0$ , and the initial pressure distribution is set to the Gaussian  $p(x, t = 0) = \exp(-(10x - 3.5)^4)$ . The time implicit simulations employ a fixed time step of  $\Delta t = 0.05$  evolving in  $N_t + 1 = 30$  time steps on a grid with  $N_p = 64$  ( $n = 6$ ) interior grid points. The pressure is encoded using the bricklayer ansatz with depth  $d = 5$ . The convergence criterion for the optimizations is  $\tau_{\text{tol}} = 10^{-7}$ , limited to a maximum number of 300 iterations.

To enforce the homogeneous Dirichlet boundary conditions, corrections of the periodic contribution from the central differences  $J_{\text{cent-2}}$  are required [23] and marked by  $J_{\text{DN}_{\text{cent-2}}}$ . Analogous to the previous cases, the second derivative w.r.t. time, cf. Eqn. (2), is attributed to a potential term  $J_P$  and source term  $J_S$ . Apart from the latter contribution to the linear form  $F(y)$ , the spatial differencing schemes are symmetric and can be realized fully implicit on the normalized time interval  $[0, 1]$ . The time evolution follows from the solution of an optimization problem for each time instant  $l$ , viz.

$$\min_{\mathbf{v}} J(\mathbf{v}), \text{ where } J(\mathbf{v}) = -a_3 \overbrace{J_{\text{cent-2}}^{(17)}} + a_3 \underbrace{J_{\text{DN}_{\text{cent-2}}}}_{\text{b.c. [23]}} + J_P + J_S. \quad (45)$$

Figure 11 illustrates the results obtained for the VQA and the classical FD approach in the previously introduced manner. The spatio/temporal evolution of the VQA-predicted pressure is displayed in Fig. 11a. Again, the abscissa refers to the spatial location and the ordinate to the time. The Figure also indicates the six time instants that are used to compare spatial velocity profiles obtained by the VQA and the classical method in Fig. 11b. On the right side, Figure 11c shows the temporal evolution of the two error measures introduced in Eqn. (38).

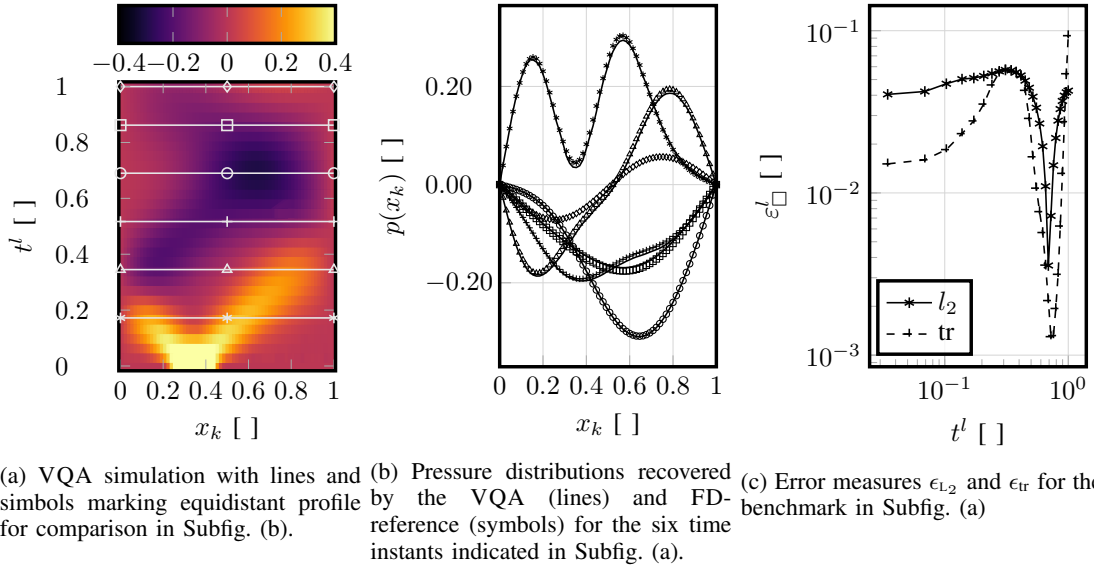


Fig. 11: Temporal evolution of the VQA results for the linear transport problem governed by the wave equation on a  $N_p = 64$  interior points subjected to Dirichlet boundary conditions and simulated for  $N_t + 1 = 30$  time steps.

The initial Gaussian distribution is clearly observed from the light color near to the ordinate in Fig. 11a. In the further course of time, the wave propagates in both directions and changes phase when being reflected at the boundaries. The reflected waves subsequently propagate in the opposite direction and interact within the third spatial quarter, resulting in a situation that is pointwise symmetric to the initial condition. As seen from Fig. 11b, the VQA results are consistent to their FD counterparts (symbols). The rightmost Fig. 11c provides quantitative evidence, showing the evolution of the error measures introduced in Eqn. (38). The Figure reveals pronounced error minima close to a level of  $10^{-3}$  when the pressure waves interact around  $t^l = 0.7$ . Thereafter, the error deteriorates again and can only be reduced by a larger depth  $d$ , which provides a more expressive ansatz. The time averaged errors for  $l_2$  and trace distance are  $\bar{\epsilon}_{l_2} = 0.037$  and  $\bar{\epsilon}_{tr} = 0.026$ , respectively.

The observed minima can be explained by the ability of the ansatz to represent Gaussian distributions, for which it is easy to optimize. The results show that the problem described by the hyperbolic linear second-order PDE can be accurately solved with the VQA on a QC.

## VI. CONCLUSION

The work presents a flexible VQA for simulating linear and nonlinear fluid dynamic transport phenomena using a hybrid classical-quantum computing framework. The method combines FD approximations for differential operators with an optimization problem that minimizes the weak formulation of the associated governing PDE. To this end, the parameters of a modular ansatz circuit are trained on the classical hardware while the expensive evaluations of the objective functional are executed on the QC.

The approach treats symmetrically discretized dynamics implicitly, while non-symmetric/biased discretizations, e.g., of the convective kinematics, are explicitly treated. It supports non-homogeneous diffusivity and the coding of classical, upwind-biased schemes of first (UDS) and higher order (e.g. LUDS, QUICK) into the quantum concept, which, in contrast to central differences, do not generate dispersion waves [25], [53] even at high *Reynolds/Péclet* numbers. The VQA results are generally in very good agreement with results obtained from classical methods.

The implementation encodes all non-zero diagonals of the discrete operators into individual QNPU and embeds them in Hadamard test-based circuits. The resulting scalar-valued multi-objective optimal control problem is constructed with only one ancilla qubit measurement per circuit and it features remarkably low circuit counts for symmetric and Toeplitz matrices which generally appear in CFD applications. The method therefore favorably distinguishes from other variational methods based upon Linear Combination of Unitaries (LCU) [54], where the number of ancillas and measurements scales with the LCU contributions. In addition, an optimal scaling in gate complexity w.r.t. the number of qubits is achieved, which is at most *polylog*, due to the efficient combination of adder and potential circuits [25].

Future work will refer to non-uniform grids, along the route outlined for the non-constant material example, and an extension to more than one spatial dimension by tensor products of the spatial discretization. Open challenges for amplitude phase estimation in terms of min / max operations will be addressed.

## ACKNOWLEDGMENT

This publication and the current work have received funding from the European Union's Horizon Europe research and innovation program (HORIZON-CL4-2021-DIGITAL-EMERGING-02-10) under grant agreement No. 101080085 QCFD.

## AUTHOR CONTRIBUTIONS

**Sergio Bengoechea:** Conceptualization, Methodology, Software, Validation, Formal analysis, Investigation, Writing - original draft, Writing - review & editing, Visualization. **Paul Over:** Conceptualization, Methodology, Software, Validation, Formal analysis, Investigation, Writing - original draft, Writing - review & editing, Visualization. **Dieter Jaksch:** Project administration, Funding acquisition, Supervision, Resources, Writing - review & editing. **Thomas Rung:** Project administration, Funding acquisition, Supervision, Conceptualization, Methodology, Resources, Writing - original draft, Writing - review & editing.

## REFERENCES

- [1] J. P. Slotnick, A. Khodadoust, J. Alonso, D. Darmofal, W. Gropp, E. Lurie, and D. J. Mavriplis, “Cfd vision 2030 study: a path to revolutionary computational aerospace,” NASA, Tech. Rep., Mar 2014. [Online]. Available: <https://ntrs.nasa.gov/citations/20140003093>
- [2] D. Jaksch, P. Givi, A. J. Daley, and T. Rung, “Variational quantum algorithms for computational fluid dynamics,” *AIAA Journal*, vol. 61, no. 5, pp. 1885–1894, Mar 2023. [Online]. Available: <https://doi.org/10.2514/1.J062426>
- [3] N. Gourianov, M. Lubasch, S. Dolgov, Q. Y. van den Berg, H. Babae, P. Givi, M. Kiffner, and D. Jaksch, “A quantum-inspired approach to exploit turbulence structures,” *Nature Computational Science*, vol. 2, no. 1, pp. 30–37, Jan 2022. [Online]. Available: <https://doi.org/10.1038/s43588-021-00181-1>
- [4] M. Kiffner and D. Jaksch, “Tensor network reduced order models for wall-bounded flows,” *Physical Review Fluids*, vol. 8, no. 12, p. 124101, Dec 2023. [Online]. Available: <https://doi.org/10.1103/physrevfluids.8.124101>
- [5] R. D. Peddinti, S. Pisoni, A. Marini, P. Lott, H. Argentieri, E. Tiunov, and L. Aolita, “Quantum-inspired framework for computational fluid dynamics,” *Communications Physics*, vol. 7, no. 1, Apr 2024. [Online]. Available: <https://doi.org/10.1038/s42005-024-01623-8>
- [6] R. Steijl and G. N. Barakos, “Parallel evaluation of quantum algorithms for computational fluid dynamics,” *Computers & Fluids*, vol. 173, Sep 2018. [Online]. Available: <https://doi.org/10.1016/j.compfluid.2018.03.080>
- [7] Y. Cao, A. Papageorgiou, I. Petras, J. Traub, and S. Kais, “Quantum algorithm and circuit design solving the Poisson equation,” *New Journal of Physics*, vol. 15, no. 1, Jan 2013. [Online]. Available: <https://doi.org/10.1088/1367-2630/15/1/013021>
- [8] A. W. Harrow, A. Hassidim, and S. Lloyd, “Quantum algorithm for linear systems of equations,” *Physical Review Letters*, vol. 103, no. 15, Oct 2009. [Online]. Available: <https://doi.org/10.1103/physrevlett.103.150502>
- [9] F. Gaitan, “Finding flows of a Navier—Stokes fluid through quantum computing,” *npj Quantum Information*, vol. 6, no. 1, Jul 2020. [Online]. Available: <https://doi.org/10.1038/s41534-020-00291-0>
- [10] F. Oz, R. K. S. S. Vuppala, K. Kara, and F. Gaitan, “Solving Burgers’ equation with quantum computing,” *Quantum Information Processing*, vol. 21, no. 1, Dec 2021. [Online]. Available: <https://doi.org/10.1007/s11128-021-03391-8>
- [11] B. Kacewicz, “Almost optimal solution of initial-value problems by randomized and quantum algorithms,” *Journal of Complexity*, vol. 22, no. 5, pp. 676–690, Oct 2006. [Online]. Available: <https://doi.org/10.1016/j.jco.2006.03.001>
- [12] Z.-Y. Chen, C. Xue, S.-M. Chen, B.-H. Lu, Y.-C. Wu, J.-C. Ding, S.-H. Huang, and G.-P. Guo, “Quantum finite volume method for computational fluid dynamics with classical input and output,” *arXiv (pre-print)*, Feb 2021. [Online]. Available: <https://doi.org/10.48550/arXiv.2102.03557>
- [13] P. Brearley and S. Laizet, “Quantum algorithm for solving the advection equation using hamiltonian simulation,” *Phys. Rev. A*, vol. 110, p. 012430, Jul 2024. [Online]. Available: <https://doi.org/10.1103/PhysRevA.110.012430>
- [14] A. Suau, G. Staffelbach, and H. Calandra, “Practical quantum computing: Solving the wave equation using a quantum approach,” *ACM Transactions on Quantum Computing*, vol. 2, no. 1, Feb 2021. [Online]. Available: <https://doi.org/10.1145/3430030>
- [15] J. Preskill, “Quantum Computing in the NISQ era and beyond,” *Quantum*, vol. 2, p. 79, Aug 2018. [Online]. Available: <https://doi.org/10.22331/q-2018-08-06-79>
- [16] O. Kyriienko, A. E. Paine, and V. E. Elfving, “Solving nonlinear differential equations with differentiable quantum circuits,” *Physical Review A*, vol. 103, no. 5, May 2021. [Online]. Available: <https://doi.org/10.1103/physreva.103.052416>
- [17] R. Demirdjian, D. Gunlycke, C. A. Reynolds, J. D. Doyle, and S. Tafur, “Variational quantum solutions to the advection–diffusion equation for applications in fluid dynamics,” *Quantum Information Processing*, vol. 21, no. 9, Sep 2022. [Online]. Available: <https://doi.org/10.1007/s11128-022-03667-7>
- [18] C. Bravo-Prieto, R. LaRose, M. Cerezo, Y. Subasi, L. Cincio, and P. J. Coles, “Variational quantum linear solver,” *Quantum*, vol. 7, p. 1188, Nov 2023. [Online]. Available: <https://doi.org/10.22331/q-2023-11-22-1188>
- [19] Y. Sato, R. Kondo, S. Koide, H. Takamatsu, and N. Imoto, “Variational quantum algorithm based on the minimum potential energy for solving the Poisson equation,” *Physical Review A*, vol. 104, no. 5, Nov 2021. [Online]. Available: <https://doi.org/10.1103/physreva.104.052409>
- [20] F. Y. Leong, W.-B. Ewe, and D. E. Koh, “Variational quantum evolution equation solver,” *Scientific Reports*, vol. 12, no. 1, Jun 2022. [Online]. Available: <https://doi.org/10.1038/s41598-022-14906-3>

- [21] F. Y. Leong, D. E. Koh, W.-B. Ewe, and J. F. Kong, “Variational quantum simulation of partial differential equations: applications in colloidal transport,” *International Journal of Numerical Methods for Heat & Fluid Flow*, vol. 33, no. 11, Jul 2023. [Online]. Available: <https://doi.org/10.1108/hff-05-2023-0265>
- [22] F. Y. Leong, D. E. Koh, J. F. Kong, S. T. Goh, J. Y. Khoo, W.-B. Ewe, H. Li, J. Thompson, and D. Poletti, “Solving fractional differential equations on a quantum computer: A variational approach,” *AVS Quantum Science*, vol. 6, no. 3, Jul 2024. [Online]. Available: <https://doi.org/10.1116/5.0202971>
- [23] P. Over, S. Bengoechea, T. Rung, F. Clerici, L. Scandurra, E. de Villiers, and D. Jaksch, “Boundary treatment for variational quantum simulations of partial differential equations on quantum computers,” *arXiv (pre-print)*, Feb 2024. [Online]. Available: <https://doi.org/10.48550/arXiv.2402.18619>
- [24] P. Over, S. Bengoechea, P. Brearley, S. Laizet, and T. Rung, “Quantum algorithm for the advection-diffusion equation with optimal success probability,” *arXiv (pre-print)*, Oct 2024. [Online]. Available: <https://doi.org/10.48550/arXiv.2410.07909>
- [25] M. Lubasch, J. Joo, P. Moinier, M. Kiffner, and D. Jaksch, “Variational quantum algorithms for nonlinear problems,” *Physical Review A*, vol. 101, no. 1, Jan 2020. [Online]. Available: <https://doi.org/10.1103/physreva.101.010301>
- [26] A. Javadi-Abhari, M. Treinish, K. Krsulich, C. J. Wood, J. Lishman, J. Gacon, S. Martiel, P. D. Nation, L. S. Bishop, A. W. Cross, B. R. Johnson, and J. M. Gambetta, “Quantum computing with qiskit,” *arXiv (pre-print)*, Jun 2024. [Online]. Available: <https://doi.org/10.48550/arXiv.2405.08810>
- [27] C. Grossmann, H.-G. Roos, and M. Stynes, *Numerical Treatment of Partial Differential Equations*. Springer Berlin Heidelberg, Aug 2007. [Online]. Available: <https://doi.org/10.1007/978-3-540-71584-9>
- [28] R. Glowinski, *Variational Methods for the Numerical Solution of Nonlinear Elliptic Problems*. Philadelphia, PA: Society for Industrial and Applied Mathematics, Nov 2015. [Online]. Available: <https://doi.org/10.1137/1.9781611973785>
- [29] J. H. Ferziger, M. Perić, and R. L. Street, *Computational Methods for Fluid Dynamics*. Springer International Publishing, Aug 2020. [Online]. Available: <https://doi.org/10.1007/978-3-319-99693-6>
- [30] M. A. Nielsen and I. L. Chuang, *Quantum Computation and Quantum Information*. Cambridge University Press, Dec 2010. [Online]. Available: <https://doi.org/10.1017/CBO9780511976667>
- [31] J. L. Troutman, *Variational Calculus and Optimal Control*. Springer New York, Sep 1996. [Online]. Available: <https://doi.org/10.1007/978-1-4612-0737-5>
- [32] D. Werner, *Funktionalanalysis*. Springer, Mar 2005. [Online]. Available: <https://doi.org/10.1007/978-3-662-55407-4>
- [33] S. Endo, Z. Cai, S. C. Benjamin, and X. Yuan, “Hybrid quantum-classical algorithms and quantum error mitigation,” *J. Phys. Soc. Jpn.*, vol. 90, no. 3, Mar 2021. [Online]. Available: <https://doi.org/10.7566/jpsj.90.032001>
- [34] N. M. Guseynov, A. A. Zhukov, W. V. Pogosov, and A. V. Lebedev, “Depth analysis of variational quantum algorithms for the heat equation,” *Physical Review A*, vol. 107, no. 5, May 2023. [Online]. Available: <http://doi.org/10.1103/physreva.107.052422>
- [35] K. Nakaji and N. Yamamoto, “Expressibility of the alternating layered ansatz for quantum computation,” *Quantum*, vol. 5, Apr 2021. [Online]. Available: <https://doi.org/10.22331/q-2021-04-19-434>
- [36] A. Sarma, T. W. Watts, M. Moosa, Y. Liu, and P. L. McMahon, “Quantum variational solving of nonlinear and multidimensional partial differential equations,” *Phys. Rev. A*, vol. 109, p. 062616, Jun 2024. [Online]. Available: <https://doi.org/10.1103/PhysRevA.109.062616>
- [37] V. Vedral, A. Barenco, and A. Ekert, “Quantum networks for elementary arithmetic operations,” *Physical Review A*, vol. 54, no. 1, Jul 1996. [Online]. Available: <https://doi.org/10.1103/physreva.54.147>
- [38] K. McDonnell, L. F. Keary, and J. D. Pritchard, “Demonstration of a quantum gate using electromagnetically induced transparency,” *Phys. Rev. Lett.*, vol. 129, p. 200501, Nov 2022. [Online]. Available: <https://doi.org/10.1103/PhysRevLett.129.200501>
- [39] B. van Leer, “Upwind-difference methods for aerodynamic problems governed by the Euler equations,” in *Large-Scale Computations in Fluid Mechanics*, B. E. Engquist, S. Osher, and R. C. J. Somerville, Eds., Jan 1985, pp. 327–336.
- [40] N. Waterson and H. Deconinck, “Design principles for bounded higher-order convection schemes – a unified approach,” *Journal of Computational Physics*, vol. 224, no. 1, pp. 182–207, May 2007. [Online]. Available: <https://doi.org/10.1016/j.jcp.2007.01.021>
- [41] R. W. Johnson and R. J. MacKinnon, “Equivalent versions of the quick scheme for finite-difference and finite-volume numerical methods,” *Communications in Applied Numerical Methods*, vol. 8, no. 12, pp. 841–847, Dec 1992. [Online]. Available: <https://doi.org/10.1002/cnm.1630081202>

- [42] P. E. Black, D. R. Kuhn, and C. J. Williams, “Quantum computing and communication,” *Advances in Computers*, vol. 56, May 2002. [Online]. Available: [https://doi.org/10.1016/S0065-2458\(02\)80007-9](https://doi.org/10.1016/S0065-2458(02)80007-9)
- [43] M. Cerezo, A. Arrasmith, R. Babbush, S. C. Benjamin, S. Endo, K. Fujii, J. R. McClean, K. Mitarai, X. Yuan, L. Cincio, and P. J. Coles, “Variational quantum algorithms,” *Nature Reviews Physics*, vol. 3, no. 9, Aug 2021. [Online]. Available: <https://doi.org/10.1038/s42254-021-00348-9>
- [44] F. Mozafari, G. De Micheli, and Y. Yang, “Efficient deterministic preparation of quantum states using decision diagrams,” *Physical Review A*, vol. 106, no. 2, p. 022617, Aug 2022. [Online]. Available: <https://doi.org/10.1103/physreva.106.022617>
- [45] F. M. Creevey, C. D. Hill, and L. C. L. Hollenberg, “GASP: a genetic algorithm for state preparation on quantum computers,” *Scientific Reports*, vol. 13, no. 1, Jul 2023. [Online]. Available: <https://doi.org/10.1038/s41598-023-37767-w>
- [46] A. A. Melnikov, A. A. Termanova, S. V. Dolgov, F. Neukart, and M. R. Perelshtein, “Quantum state preparation using tensor networks,” *Quantum Science and Technology*, vol. 8, no. 3, Jun 2023. [Online]. Available: <https://doi.org/10.1088/2058-9565/acd9e7>
- [47] I. F. Araujo, D. K. Park, F. Petruccione, and A. J. da Silva, “A divide-and-conquer algorithm for quantum state preparation,” *Scientific Reports*, vol. 11, no. 1, Mar 2021. [Online]. Available: <https://doi.org/10.1038/s41598-021-85474-1>
- [48] J. Nocedal and S. J. Wright, *Numerical optimization*, 2nd ed. New York, NY: Springer, Jul 2006. [Online]. Available: <https://doi.org/10.1007/978-0-387-40065-5>
- [49] M. Schuld, V. Bergholm, C. Gogolin, J. Izaac, and N. Killoran, “Evaluating analytic gradients on quantum hardware,” *Physical Review A*, vol. 99, no. 3, Mar 2019. [Online]. Available: <https://doi.org/10.1103/physreva.99.032331>
- [50] L. Banchi and G. E. Crooks, “Measuring analytic gradients of general quantum evolution with the stochastic parameter shift rule,” *Quantum*, vol. 5, Jan 2021. [Online]. Available: <https://doi.org/10.22331/q-2021-01-25-386>
- [51] G. E. Crooks, “Gradients of parameterized quantum gates using the parameter-shift rule and gate decomposition,” *arXiv (pre-print)*, Nov 2019. [Online]. Available: <https://doi.org/10.48550/arXiv.1905.13311>
- [52] B. P. Leonard, “Simple high-accuracy resolution program for convective modelling of discontinuities,” *International Journal for Numerical Methods in Fluids*, vol. 8, no. 10, pp. 1291–1318, Oct 1988. [Online]. Available: <https://doi.org/10.1002/fld.1650081013>
- [53] F. Guzman-Cajica and F. S. Guzmán, “Variational quantum crank-nicolson and method-of-lines schemes for the solution of initial value problems,” *Phys. Rev. A*, vol. 110, p. 042415, Oct 2024. [Online]. Available: <https://doi.org/10.1103/PhysRevA.110.042415>
- [54] S. T. Crowe, R. Rodriguez, D. Gunlycke, F. Escobar, and J. N. Ptasinski, “Efficient embedding to solve the quantum linear systems problem in near-term quantum processors,” in *Quantum Communications and Quantum Imaging XX*, K. S. Deacon and R. E. Meyers, Eds., vol. 12238, International Society for Optics and Photonics. SPIE, Oct 2022, p. 122380A. [Online]. Available: <https://doi.org/10.1117/12.2632069>